

AD-A120 016 TEXAS INSTRUMENTS INC DALLAS EQUIPMENT GROUP  
INVESTIGATION OF AN EXPLORATORY DEVELOPMENT MODEL OF THE 3HE FR—ETC(U)  
FEB 82 D D MCGREGOR

F/6 20/3

N60921-81-C-0264

NL

UNCLASSIFIED

[or]  
ADA  
20016

END  
DATE  
FILED  
11-82  
OTC

AD A120016

DTIC FILE COPY

FINAL REPORT

INVESTIGATION OF AN EXPLORATORY  
DEVELOPMENT MODEL OF THE  $^3\text{He}$   
FREE PRECESSION GRADIOMETER

26 FEBRUARY 1982

CONTRACT N60921-81-C-0264

This document has been approved  
for public release and sale; its  
distribution is unlimited.



A

82 10 07 031

FINAL REPORT

INVESTIGATION OF AN EXPLORATORY  
DEVELOPMENT MODEL OF THE  $^3\text{He}$   
FREE PRECESSION GRADIOMETER

26 FEBRUARY 1982

CONTRACT N60921-81-C-0264

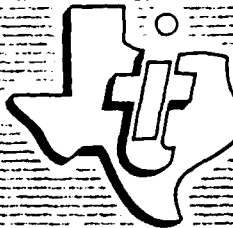
PREPARED FOR:

Naval Surface Weapons Center  
White Oak  
Silver Springs, Maryland 20190

PREPARED BY:

Equipment Group  
Dallas, Texas

*Douglas D. McGregor*  
Dr. Douglas D. McGregor



**TEXAS INSTRUMENTS**  
INCORPORATED

UNCLASSIFIED

SECURITY CLASSIFICATION OF THIS PAGE (When Data Entered)

DD FORM 1 JAN 73 1473 EDITION OF 1 NOV 68 IS OBSOLETE  
S/N 0102-LF-014-6601

**UNCLASSIFIED**

## TABLE OF CONTENTS

SECTION	TITLE	PAGE
1	INTRODUCTION .....	1
2	CHARACTERISTICS OF XDM $^3\text{He}$ FREE PRECESSION GRADIOMETER .....	2
3	ORIENTATION DEPENDENCE OF XDM $^3\text{He}$ MAGNETOMETERS .....	19
4	EFFECT OF MAGNETIC MOMENT PROXIMITY .....	27
5	MOVING DIPOLE DETECTION TEST .....	32
6	SUMMARY .....	46
7	RECOMMENDATIONS .....	47
Appendix A	WORK STATEMENT .....	50
Appendix B	$^3\text{He}$ GRADIOMETER PERFORMANCE ANALYSIS METHODOLOGY	52
	References .....	59



## LIST OF TABLES

TABLE NO.	TITLE	PAGE
1	Automatic Pump Sequence .....	6
7.1.	Program Tasks Outline .....	48
B.1	.....	56
B.2	.....	56
B.3	.....	57
B.4	.....	58

## LIST OF ILLUSTRATIONS

FIGURE	TITLE	PAGE
1	Block Diagram of XDM $^3\text{He}$ Gradiometer Sensors and Support Electronics .....	3
2	Drawing of the XDM $^3\text{He}$ Free Precession Magnetometer .....	4
3	Photograph of one of the XDM $^3\text{He}$ Free Precession Gradiometers .....	7
4	Block Diagram of Automatic Pump Sequencer System .....	8
5	Block Diagram of Frequency Discriminator System .....	9
6	Transfer Function for Amplifiers to Sensor Pickup Coils .....	11
7	Plot of the Asymptotic Signal Level $S_0$ Versus Pumping Time Constant $T_1$ for 2 Inch Diameter 10 Torr Cell of XDM $^3\text{He}$ Gradiometer .....	12
8	Noise Power Spectral Density of XDM $^3\text{He}$ Gradiometer. 0 dB = 1 Gamma $^2/\text{Hz}$ . Natural frequency of phase locked loops is 0.4 Hz. Gradiometer signal-to-noise parameter is 42.2 dB-Hz. The sensors are oriented along Earth's magnetic field .....	15
9	Noise Power Spectral Density of XDM $^3\text{He}$ Gradiometer. 0 dB = 1 Gamma $^2/\text{Hz}$ . The conditions are the same as for Figure 8 .....	16
10	Noise Power Spectral Density of XDM $^3\text{He}$ Gradiometer. 0 dB = 1 Gamma $^2/\text{Hz}$ . Natural frequency of phase locked loops is 0.1 Hz. Gradiometer signal-to-noise parameter is 42.9 dB-Hz. The sensors are oriented for a vertical pump.....	18
11	Sketch Showing the Three Axes of the $^3\text{He}$ Free Precession Magnetometer .....	20
12	Plot of $\sin \theta$ and $\cos \theta$ as a Function of the Parameter $\epsilon$ . The angle $\theta$ is the angle between the cell moment and the ambient field after rotation .....	21
13	A Plot of the Quantity $F(\theta_X)$ , the Fraction of the Polarization along $H_0$ which is Rotated into the Precession Plane, as a Function of $\theta_X$ .....	23
14	Plot of Signal Amplitude from Sensor Pickup Coils as a Function of Pumping Light Direction Relative to the Vertical. The sensor was rotated about the Helmholtz coil axis, which was directed along an east-west Line ...	25

## LIST OF ILLUSTRATIONS

FIGURE	TITLE	PAGE
15	Plot of Signal Amplitude from Sensor Pickup Coils as a Function of Pumping Light Direction relative to the Vertical. The sensor was rotated about the Helmholtz coil axis, which was directed along an east-west line ...	26
16	Sketch showing placement of $^3\text{He}$ Free Precession Sensor and Magnetic Gradient Producing Coils. The coils are located 3 feet from the sensor and are oriented with their axes either parallel with the Earth's field (along the z axis) or perpendicular to the Earth's Field (along the y axis) .....	30
17	The Free Precession Relaxation Time $T_{2\text{vH}}$ versus the Magnetic Gradient $\partial H_z / \partial x$ . The natural relaxation time has been removed from the experimental points (marked as circles and squares) .....	31
18	Block Diagram for Moving Dipole Detection Test .....	33
19	Conditions for the Moving Magnetic Dipole Test. For this test the magnetic moment was $0.96 \times 10^5$ G-cm $^3$ . The magnetic dipole was carried at 7.5 ft/sec (4.44 Knot)....	35
20	Plot of Theoretical Gradiometer Signal as a Function of Distance along Path (and Time) .....	36
21	Spectrum of XDM $^3\text{He}$ Gradiometer Noise taken during Detection Test. No target signal was present during spectrum time interval. 0 dB = 1 Gamma $^2/\text{Hz}$ . The sensors were oriented for vertical pumping .....	37
22	Transfer Functions of the Digital Bandpass Filters used in Processing of Gradiometer Signal .....	38
23	Chart Recording of Gradiometer Signal Passed Through Filter 1. The time corresponding to the point of closest approach of magnet to Gradiometer is marked CPA..	40
24	Chart Recording of Gradiometer Noise Passed Through Filter 1. ....	41
25	Chart Recording of Gradiometer Signal Passed Through Filter 2 .....	42
26	Chart Recording of Gradiometer Noise Passed Through Filter 2 .....	43
27	Plot of False Alarm Rate as a Function of Threshold Setting. The squares and circles denote experimental points .....	44
B-1	$^3\text{He}$ Performance Prediction Curves .....	55

## SECTION 1 INTRODUCTION

This report describes the results of an investigation of an exploratory development model (XDM) of the  $^3\text{He}$  free precession gradiometer. The gradiometer system discussed in this report is intended for use in a mine application and could serve as an independent mine influence trigger or as the passive alert detection component of a mine system which also contains an active acoustical detection system. The investigation included the construction and evaluation of the XDM  $^3\text{He}$  gradiometer, an experiment to assess the effect of magnetic gradients on the operation of the  $^3\text{He}$  magnetometers, and a detection test in which a magnet of known strength was carried in a straight line path past the gradiometer.

The report is organized into six sections following the introductory section. A discussion of the characteristics of the XDM  $^3\text{He}$  free precession gradiometer is presented in Section 2. Included in this section are descriptions of the sensor and electronics, and the results of sensitivity measurements. In Section 3 an analysis of the orientation dependence of the magnetometer is presented along with the results of an experiment to demonstrate the orientation dependence. The presence of a magnetic moment in the proximity of the  $^3\text{He}$  magnetometer is known to reduce the free precession time. An experiment to measure this effect is discussed in Section 4. Section 5 describes a detection test of the XDM  $^3\text{He}$  gradiometer in which a magnetic dipole is moved past the gradiometer at some distance. A series of statements which summarize the findings of the effort performed under the contract are listed in Section 6. Recommendations for future work, found in Section 7, conclude the report.\*

---

\*In Appendix A the work statement of the contract is provided. Appendix B contains a description of the quadratic signal processing technique.

SECTION 2  
CHARACTERISTICS OF XDM  $^3\text{He}$  FREE PROGRESSION  
GRADIOMETER

2.1 Introduction

In this section we present the characteristics of the XDM  $^3\text{He}$  free precession gradiometer. The section begins with a description of the sensor and a discussion of the reasons behind various features of the sensor. The support electronics are next considered, with particular emphasis on the automatic pump sequencer and the frequency discriminator. Internal parameters of the gradiometer such as cell relaxation times and signal levels have been measured; the results are presented. The last part of this section deals with gradiometer sensitivity.

2.2 Description of Sensor

The block diagram of Figure 1 shows the relationship of the sensors to the support electronics. Each sensor has three inputs, one from the ignition oscillator (which drives the cell discharge), one from the lamp exciter (which drives the lamp oscillator), and one from the automatic pump sequencer which carries the frequency ramp signal to the sensor Helmholtz coil to rotate the cell moment. The output of the sensor is the precession voltage from the pickup coils. The sketch of the sensor in Figure 2 shows the various components of the sensor. A cell of spherical shape was chosen instead of a cylindrical cell because the spherical cell is less sensitive to magnetic gradients, which tend to reduce the cell free precession relaxation time. This is discussed further in Section 4. The cells were fabricated at Texas Instruments and are 2 inches in diameter, 10 Torr in pressure, and are made of 1723 aluminosilicate glass. Two 2400 turn pickup coils detect the magnetic signal of the precessing cell moment. The light to polarize the cell is provided by two  $^4\text{He}$  lamps, one above and one below the cell. Two lamps, which are driven at a reduced level from that of previous one-lamp sensors<sup>1</sup>, produce adequate cell polarization and are more reliable than one lamp. The 5-inch 10 turn Helmholtz coil is used for moment rotation.

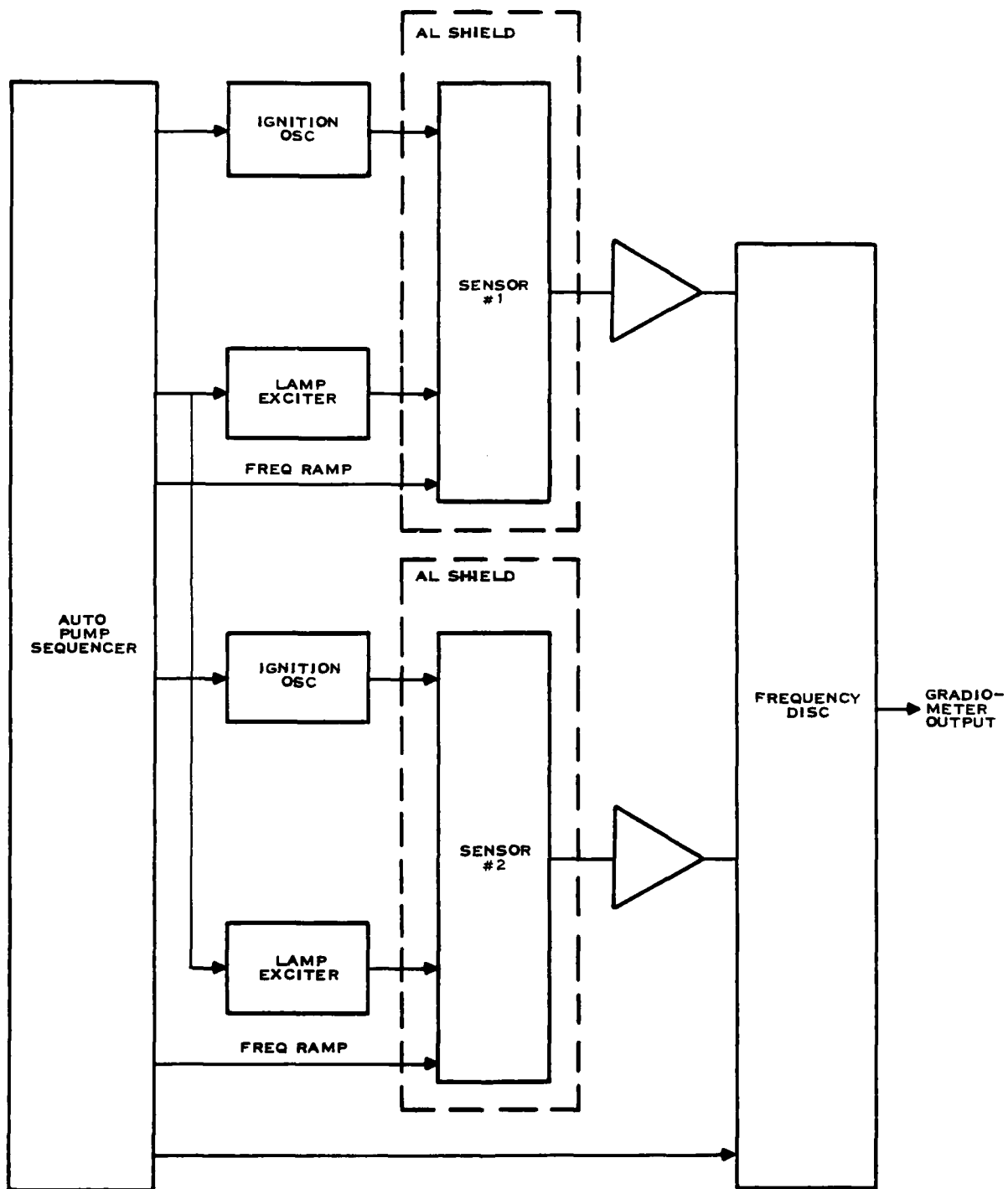


FIGURE 1. BLOCK DIAGRAM OF XDM-<sup>3</sup>He GRADIOMETER  
SENSORS AND SUPPORT ELECTRONICS.

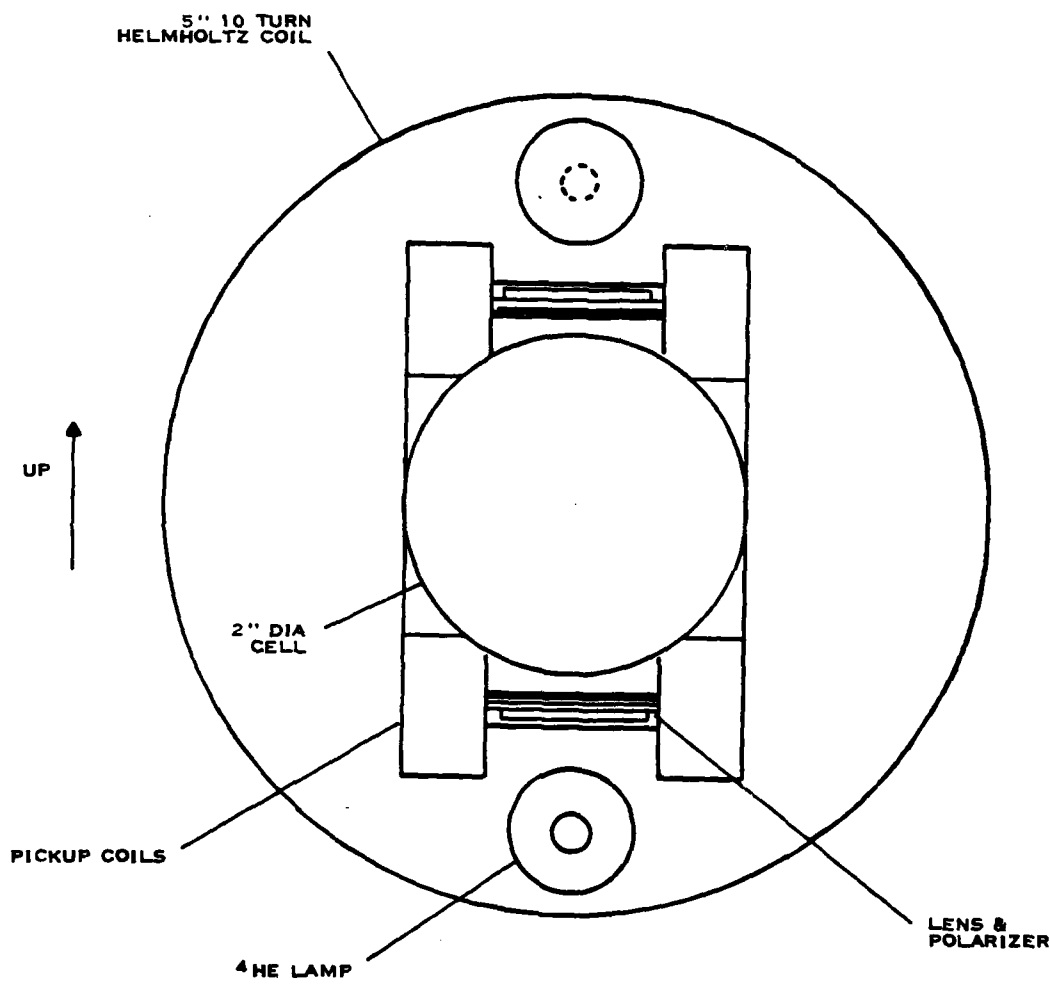


FIGURE 2. DRAWING OF THE XDM  $^3\text{He}$  FREE PRECESSION MAGNETOMETER

## 2.2 Continued

A photograph of the sensor is presented in Figure 3. The cell and lamp matching networks are visible on the top. The lamp reflectors can be seen on the lower left and upper right. The scale of the sensor in Figure 3 is established by the 5-inch diameter of the Helmholtz coil. The plates holding the pickup coils, which penetrate the plane of the Helmholtz coils, are 3.5 inch in diameter.

## 2.3 Description of Electronics

The various functional components of the support electronics are indicated in the block diagram of Figure 1.

The ignition oscillators, and lamp excitors and aluminum shields were used in an earlier contract effort and are discussed in Reference 1. For the present investigation the ignition oscillator frequency was lowered to approximately 27 kHz and the lamp exciter regulator was adjusted so that 10 W of RF power went to both lamps. A block diagram describing the functions of the automatic pump sequencer is given in Figure 4. The automatic pump sequencer controls the lamp and cell oscillators and contains a frequency ramp generator for the moment rotation. Table 1 contains a listing of the states of the automatic pump sequencer. After the initiation command the ignition oscillator (for each sensor) comes on at a high level to ignite the cell and lamp discharge. At state 3 (the pumping stage) the lamp exciter begins operation and the ignition oscillator output drops to the preset level chosen for the desired cell discharge level. Following the 320 sec pump the lamp and cell discharges are extinguished, and the frequency ramp signal (covering the interval 1400 to 2100 Hz) is directed to the Helmholtz coil. The components of the frequency discriminator are shown in Figure 5. The locking of the digital phase locked loop, contained in the frequency discriminator, to the precession signal is accomplished in several stages. An initial fast sweep of the digitally controlled oscillator frequency is made to obtain the value of the precession frequency to within an approximately 40 Hz interval. Next a slow sweep is performed through

TABLE 1. AUTOMATIC PUMP SEQUENCE

STATE	TIME INTERVAL
1. BEGIN	10 SEC
2. IGNITION	5 SEC
3. PUMP	320 SEC
4. MOMENT ROTATION	10 SEC
5. WAIT	10 SEC
6. LOCKING OF PHASE LOCKED LOOP	
(1) PRELOCK	
(2) FAST SWEEP	10 SEC*
(3) SLOW SWEEP	50 SEC*
(4) LOOP CLOSED	
7. WAIT	10 SEC
8. LOOP SETTLING	10 SEC
9. GRADIOMETER OPERATION	

The asterisks (\*) denote typical values.



FIGURE 3. PHOTOGRAPH OF ONE OF THE XDM  $^3\text{He}$  FREE PREcession MAGNETOMETERS

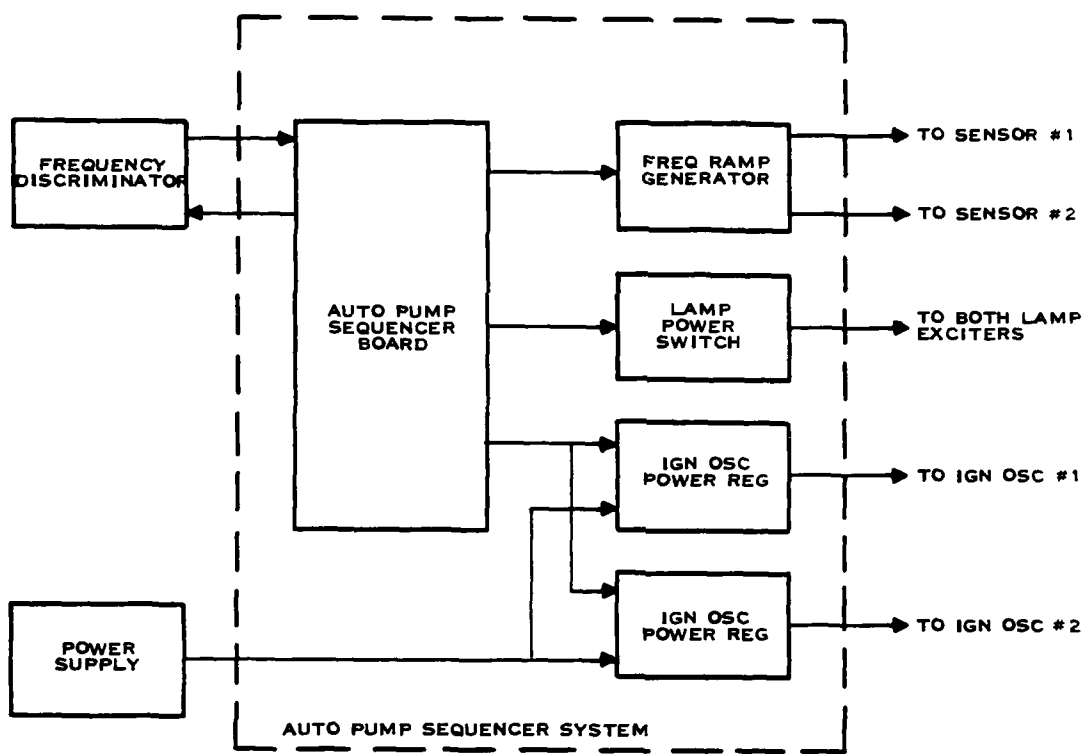


FIGURE 4. BLOCK DIAGRAM OF AUTOMATIC PUMP SEQUENCER SYSTEM

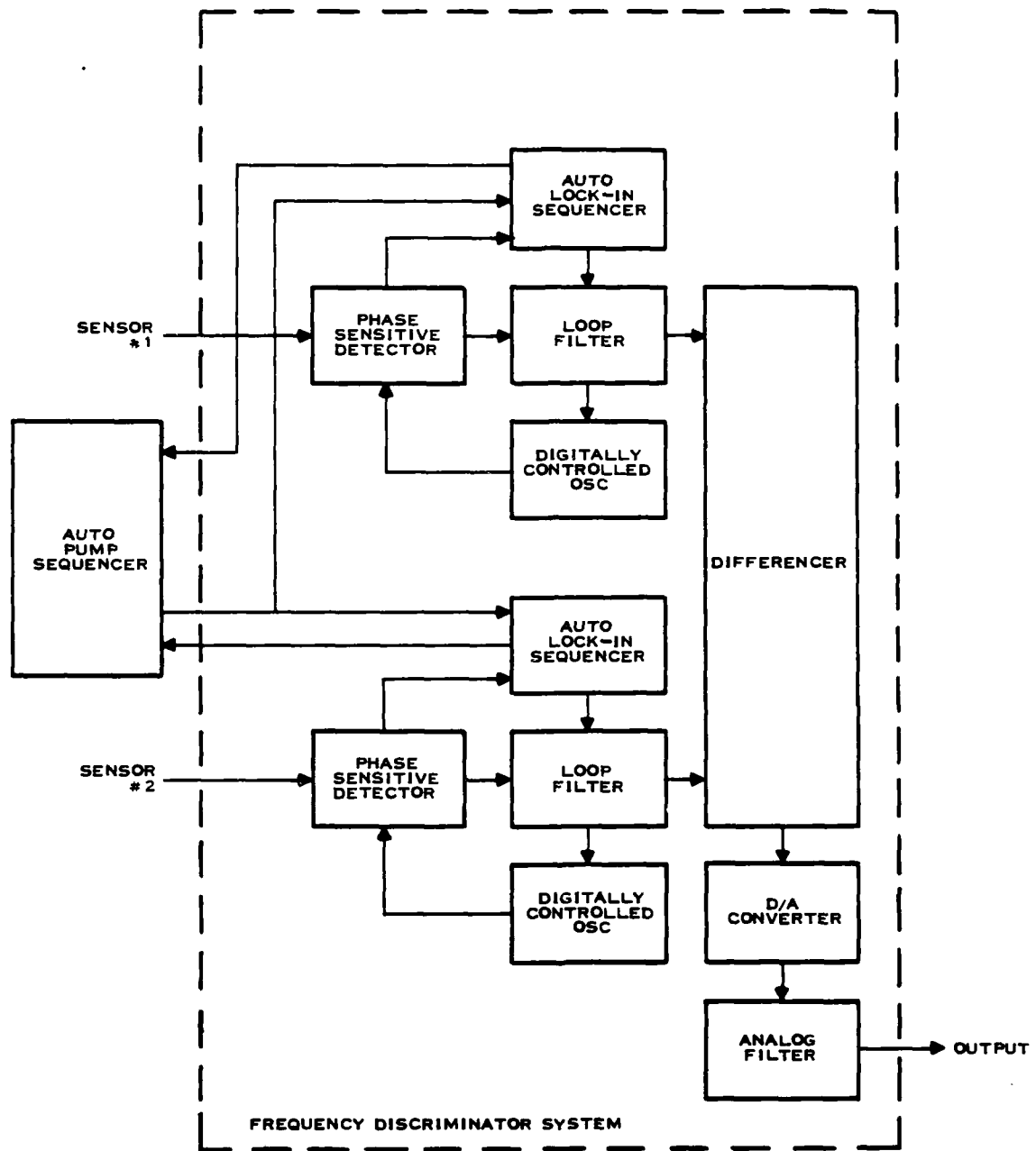


FIGURE 5. BLOCK DIAGRAM OF FREQUENCY DISCRIMINATOR SYSTEM

### 2.3 Continued

the 40 Hz interval. When the precession frequency is detected (by monitoring the phase sensitive detector), the loop is closed. Following this, a loop filter parameter which determines the bandpass of the discriminator is changed from its initial wide-open value to a preselected value (which corresponds to a reduced bandpass). After a few seconds for the loop to settle down, the gradiometer output is available for use. Approximately 435 seconds are required for the total pumping, moment rotation, and frequency locking operation.

The amplifiers to the sensor pickup coils have gains of 83.8 dB and 81.5 dB at 1725 Hz. The frequency response of the amplifier is shown in Figure 6. The bandpass characteristic of the amplifier eliminates most of the 60 Hz pickup. The precession frequencies corresponding to magnetic fields of 0.25 G and 0.75 G are indicated as dotted lines in Figure 6. The equivalent input noise levels of the amplifiers are 1.9 and 3.0 nV/  $\sqrt{\text{Hz}}$ . These values are of the same order as the Johnson noise associated with the pickup coil resistance, which is 2.3 nV/  $\sqrt{\text{Hz}}$ . Conventional power supplies are used to power the oscillators and digital electronics; for the amplifiers, batteries are used.

### 2.4 Relaxation Times

The time necessary to polarize the cell during the pumping process can be determined by measurement of the cell's longitudinal relaxation time  $T_1$  (with the cell discharge on). A plot of the measured pickup coil asymptotic signal level versus  $T_1$  for the two sensors is presented in Figure 7. The greater values of the  $T_1$  correspond to weaker cell discharge levels. The values of  $S_0$  and  $T_1$  for a given discharge level are found by measuring the pickup signal level  $S_n$  for a set of pumping times  $t_n$ . A least-mean-square algorithm is applied to fit the measured  $S_1$  and  $T_1$  to the equation

$$S_1 = S_0 (1 - e^{-\frac{t_1}{T_1}}) \quad (2-1)$$

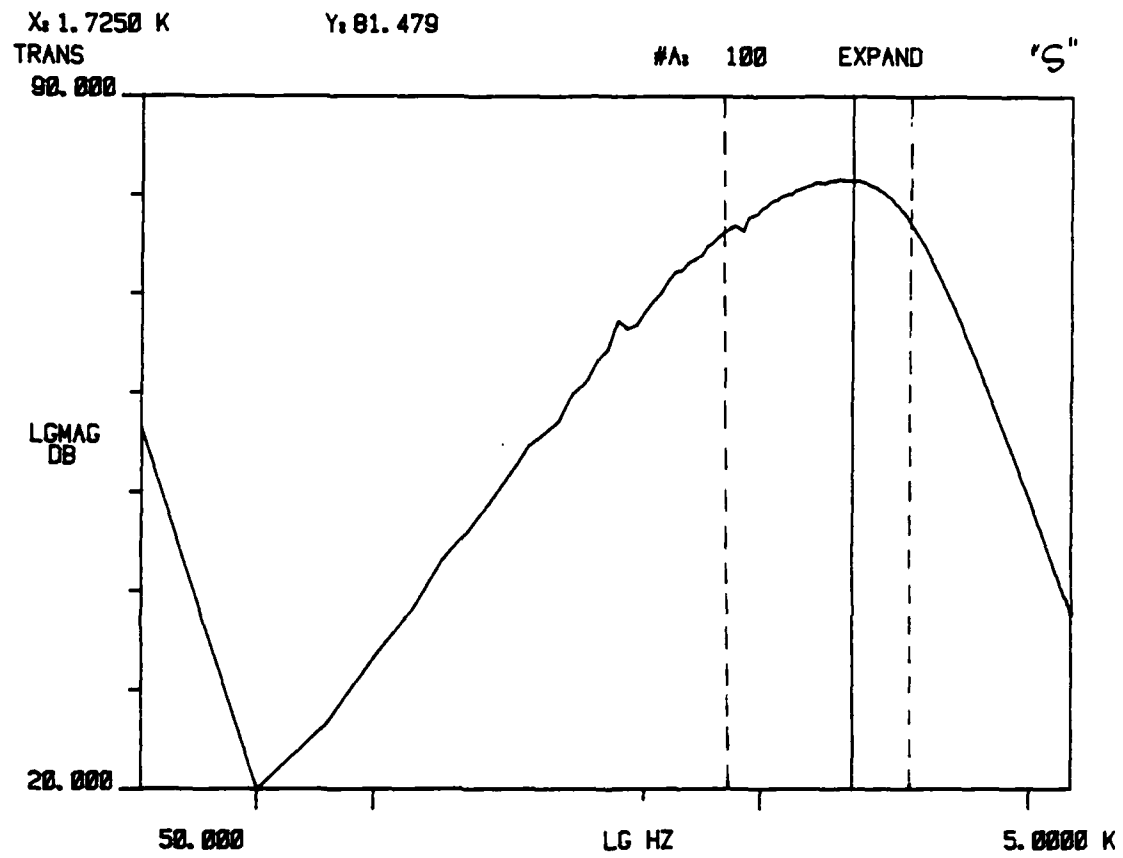


FIGURE 6. TRANSFER FUNCTION FOR AMPLIFIERS TO SENSOR PICKUP COILS

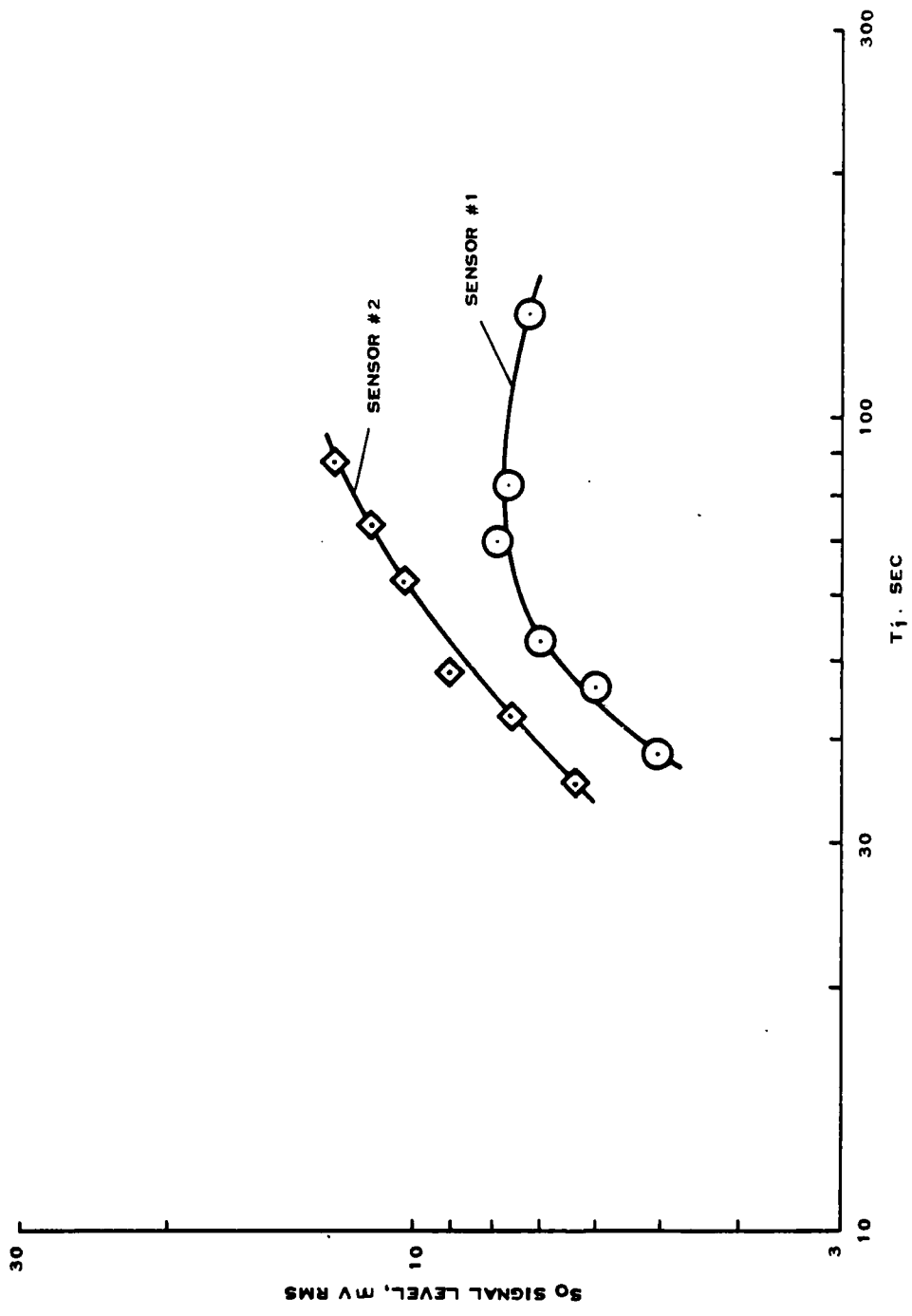


FIGURE 7. PLOT OF THE ASYMPTOTIC SIGNAL LEVEL  $S_0$  VERSUS PUMPING TIME CONSTANT  $T_1$  FOR 2 INCH DIAMETER 10 TORR CELLS OF XDM  $^3\text{He}$  GRADIOMETER

## 2.4 Continued

by adjusting  $S_0$  and  $T_1$ . The principal importance of Figure 7 is that the  $T_1$  corresponding to the largest  $S_0$  is about 85 sec for both sensors. Since the pumping period is 320 sec, we see from equation (2-1) that about 98% of the possible polarization is attained during the pump period. The difference in shapes of the two curves of Figure 7 is probably due to slightly different cell shapes and electrode patterns.

A number of measurements have been performed of the sensors' free precession relaxation times. In order to check the two sensors for magnetic cleanliness the Rice University cell with a measured 79 hour relaxation time was placed into sensor #1 and sensor #2. A  $T_2$  of 48.6 hour was obtained for sensor #1 and 63.0 hour for sensor #2. When Texas Instruments-produced 1723 aluminosilicate cells were placed in the sensors, the  $T_2$ 's were found to be 20.4 hour (for sensor #1) and 12.4 hour (for sensor #2). Later measurements yielded a  $T_2$  for sensor #1 of 16.9 hour and  $T_2$  for sensor #2 of 15.2 hour. The reasons for the variation in the  $T_2$  data have not been identified but may be due in part to slight changes in amplifier gains.

## 2.5 Gradiometer Sensitivity

The theoretical expression for a signal  $^3\text{He}$  magnetometer noise is<sup>1</sup>

$$S_n(f) = \frac{8\pi^2 N_0 f^2}{\gamma_n^2 A^2} \quad (2-2)$$

where  $S_n(f)$  is the unilateral noise spectrum,  $N_0$  is the noise spectral level at the precession frequency going into the frequency discriminator,  $f$  is the noise frequency,  $\gamma_n$  ( $= 0.203795 \text{ gamma}^{-1} \text{ sec}^{-1}$ ) is the gyromagnetic ratio for  $^3\text{He}$ , and  $A$  is the amplitude of the  $^3\text{He}$  precession signal going into the discriminator (such that the  $^3\text{He}$  precession signal is of the form  $A \cos \gamma_n H_0 t$ ). The quantities  $A$  and  $S_1$  of equation (2-1) are related by  $A^2/2 = S_1^2$ . The pickup coil

## 2.5 Continued

signal-to-noise parameter  $A^2/2N_0$  typically lies between 40 and 50 dB-Hz. For a gradiometer the (unilateral) noise spectrum is given by

$$S_n(f) = \frac{4\pi^2 f^2}{\gamma_h^2} \left\{ \left( \frac{2N_0}{A^2} \right)_1 + \left( \frac{2N_0}{A^2} \right)_2 \right\} = \frac{4\pi^2 f^2}{\gamma_h^2} \left( \frac{2N_0}{A^2} \right)_{\text{eff}} \quad (2-3)$$

where  $(A^2/2N_0)_1$  and  $(A^2/2N_0)_2$  are the signal-to-noise parameters of sensors 1 and 2, and  $(A^2/2N_0)_{\text{eff}}$  is an effective signal-to-noise parameter which characterizes the gradiometer.

Figure 8 is the measured noise spectrum of the XDM  $^3\text{He}$  gradiometer. For this experiment the sensor pump light direction was aligned with the Earth's field. The  $f^2$  sensor noise of equation (2-3) is apparent. For Figure 8  $(A^2/2N_0)_1 = 48.3$  dB-Hz  $(A^2/2N_0)_2 = 43.5$  dB-Hz and hence the effective signal-to-noise parameter is 42.2 dB-Hz. The natural frequency of the digital phase locked loops of the frequency discriminator characterizes the response of frequency discriminator. For the conditions of Figure 8 the natural frequency was about 0.4 Hz; the roll-off of the noise spectrum above 0.4 Hz is visible. The frequency discriminator permits selection of the natural frequency from among the values 0.0246, 0.0986, 0.394 and 1.58 Hz.

The noise spectrum of Figure 9 (with a smaller displayed frequency interval) shows that the low frequency noise (below 10 mHz) is present for the XDM  $^3\text{He}$  gradiometer as it was for an earlier gradiometer<sup>1</sup>. This measurement was made for the same conditions as those of Figure 7. The origin of the low frequency noise has not been identified.

In another experiment the sensors were oriented with the pumping light in the vertical direction, which is about 27 degrees from the Earth's field (at Sherman, Texas). The nominal orientation of the XDM  $^3\text{He}$  gradiometer for mine applications is that of vertical pumping. We will see in Section 3 that a vertically oriented sensor suffers a 2 dB reduction in the signal-to-noise parameter from the same sensor aligned with the Earth's field. The gradiometer

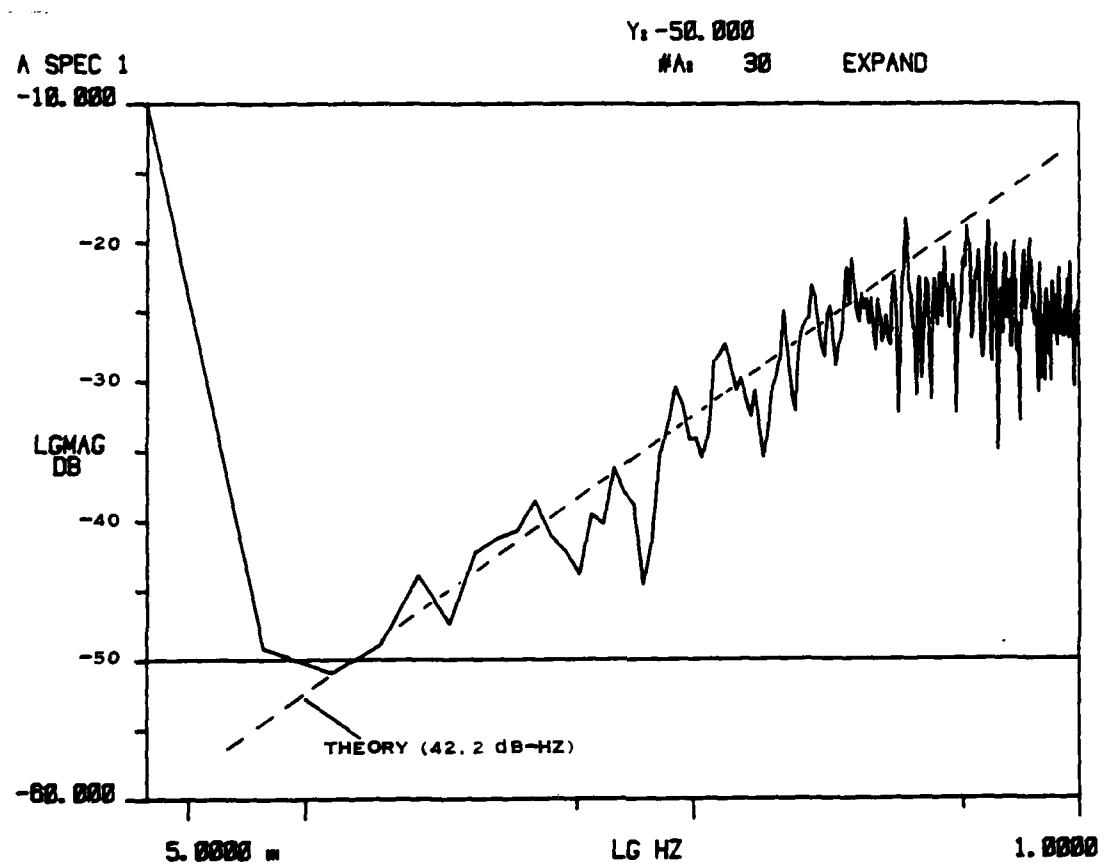


FIGURE 8. NOISE POWER SPECTRAL DENSITY OF XDM  $^3\text{He}$  GRADIOMETER.  
 0 dB = 1 GAMMA  $^2/\text{HZ}$ . NATURAL FREQUENCY OF PHASE LOCKED LOOPS IS  
 0.4 HZ. GRADIOMETER SIGNAL-TO-NOISE PARAMETER IS 42.2 dB-HZ.  
 THE SENSORS ARE ORIENTED ALONG EARTH'S MAGNETIC FIELD

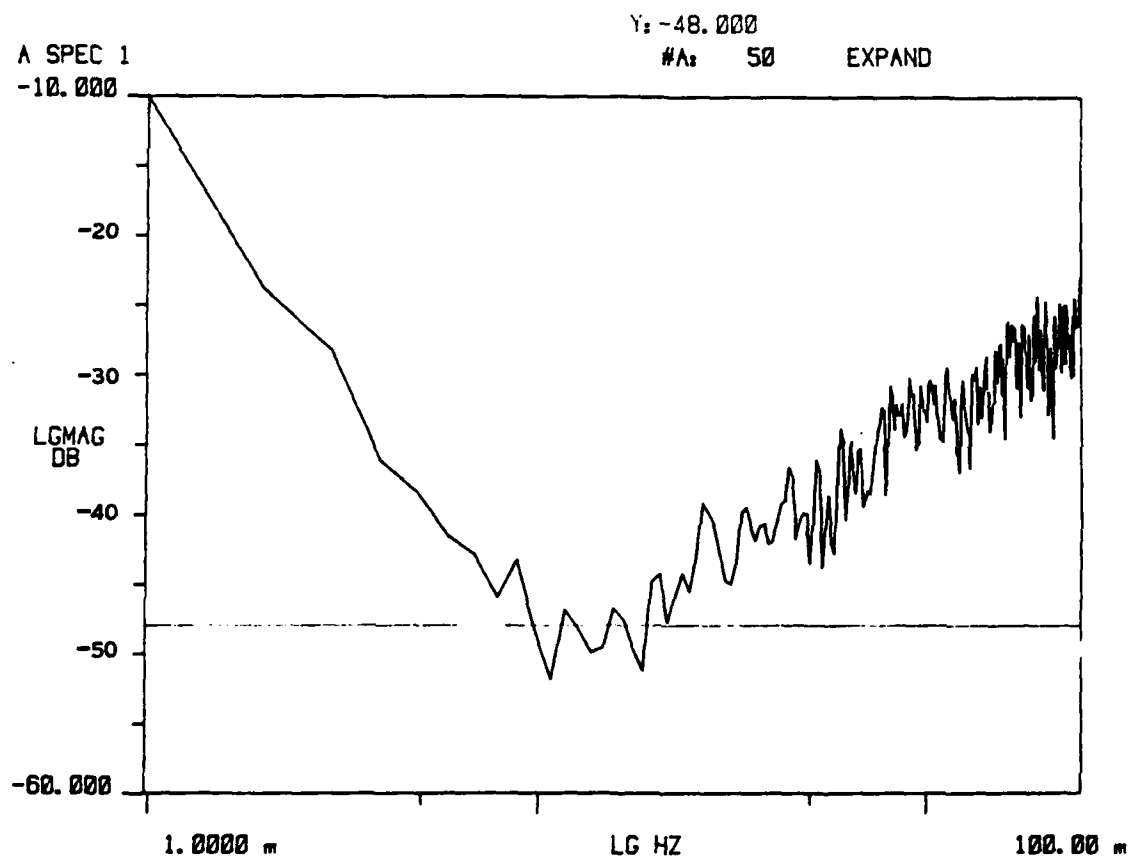


FIGURE 9. NOISE POWER SPECTRAL DENSITY OF XDM  $^3\text{He}$  GRADIOMETER.  
0 dB = 1 GAMMA $^2$ /HZ. THE CONDITIONS ARE THE SAME AS FOR FIGURE 8.

## 2.5 Continued

noise spectrum is exhibited in Figure 10. The roll-off of the spectrum at 0.1 Hz, the natural frequency, is apparent. The effective signal-to-noise parameter for the measurement was 42.9 dB-Hz.

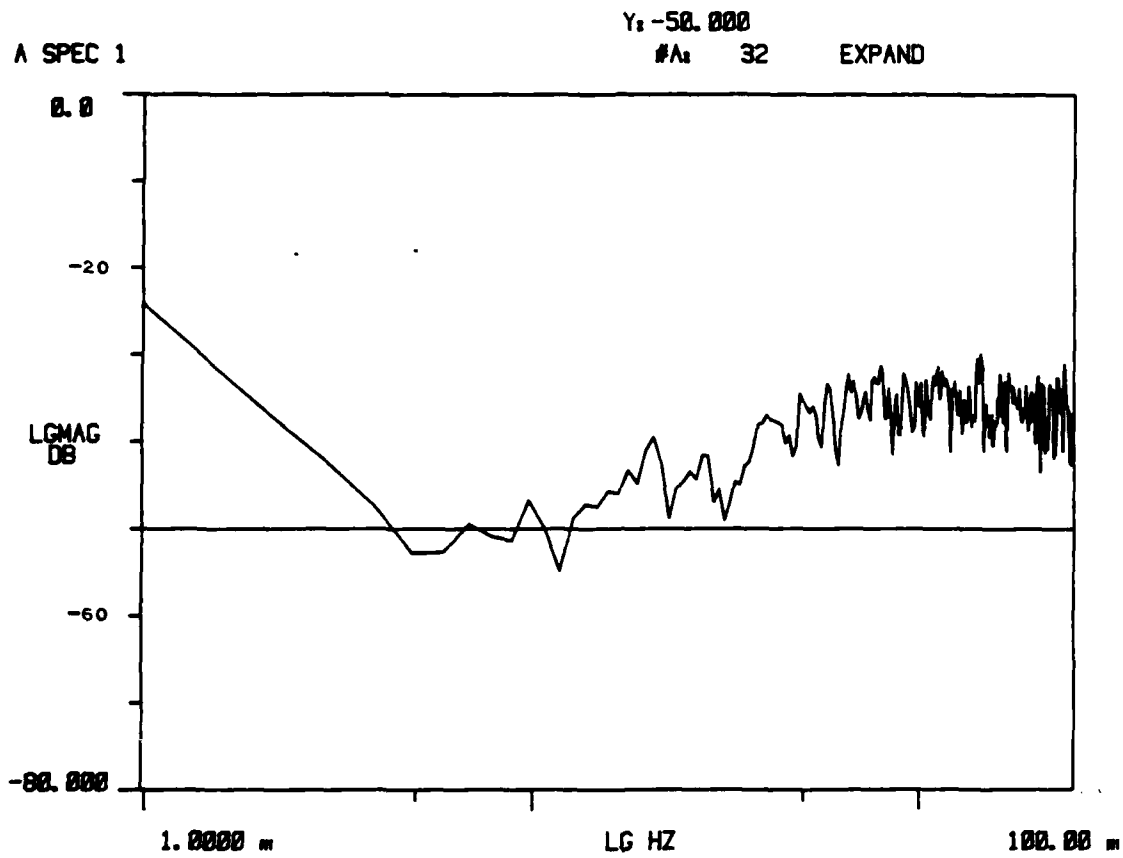


FIGURE 10. NOISE POWER SPECTRAL DENSITY OF XDM  $^3\text{He}$  GRADIOMETER.  
 0 dB = 1 GAMMA  $^2/\text{HZ}$ . NATURAL FREQUENCY OF PHASE LOCKED LOOPS IS 0.1 HZ.  
 GRADIOMETER SIGNAL-TO-NOISE PARAMETER IS 42.9 dB-HZ. THE SENSORS ARE  
 ORIENTED FOR A VERTICAL PUMP

## SECTION 3

### ORIENTATION DEPENDENCE OF XDM $^3\text{He}$ MAGNETOMETERS

#### 3.1 Introduction

The optimum orientation of the XDM  $^3\text{He}$  magnetometer is defined as the orientation which corresponds to a maximum sensor signal-to-noise parameter. This occurs when the pumping light axis is aligned along the Earth's field direction. Since the XDM  $^3\text{He}$  magnetometers are, according to plan, going to be used in an application in which it is not convenient to orient the sensors along the Earth's field, we consider in this section the orientation dependence of the sensors. A discussion of the theory of the orientation dependence is first presented, then experimental results are given.

#### 3.2 Theory of Orientation Dependence

The sketch of Figure 11 indicates the three perpendicular directions which characterize the  $^3\text{He}$  magnetometer. We label the Helmholtz coil axis as the  $x$  direction, the pickup coil axis as the  $y$  direction, and the pumping light direction as the  $z$  direction. For the planned application of the sensor, the  $z$  axis is vertical. The position of the Earth's field  $H_0$  is defined by the angles  $\theta_x$ ,  $\theta_y$ , and  $\theta_z$ , where  $\theta_i$  is the angle between the Earth's field and the  $i$ th axis.

We observe that the sensor orientation influences the signal level during the pumping stage, the flipping stage, and the free precession stage. If  $P_0$  is the cell polarization attained after pumping with  $H_0$  along the  $z$  axis, then the cell polarization that occurs for an arbitrary direction of  $H_0$  is  $P_0 \cos \theta_z$ , with the direction of the polarization along  $H_0$ . The fraction of the polarization which is precessing (i.e., in the plane perpendicular to  $H_0$ ) after the moment rotation may be calculated with the aid of Figure 12, which is taken from Reference 2. The curve labeled  $\sin \theta$  in Figure 12 represents the precessing moment amplitude (after rotation) as a function of the parameter

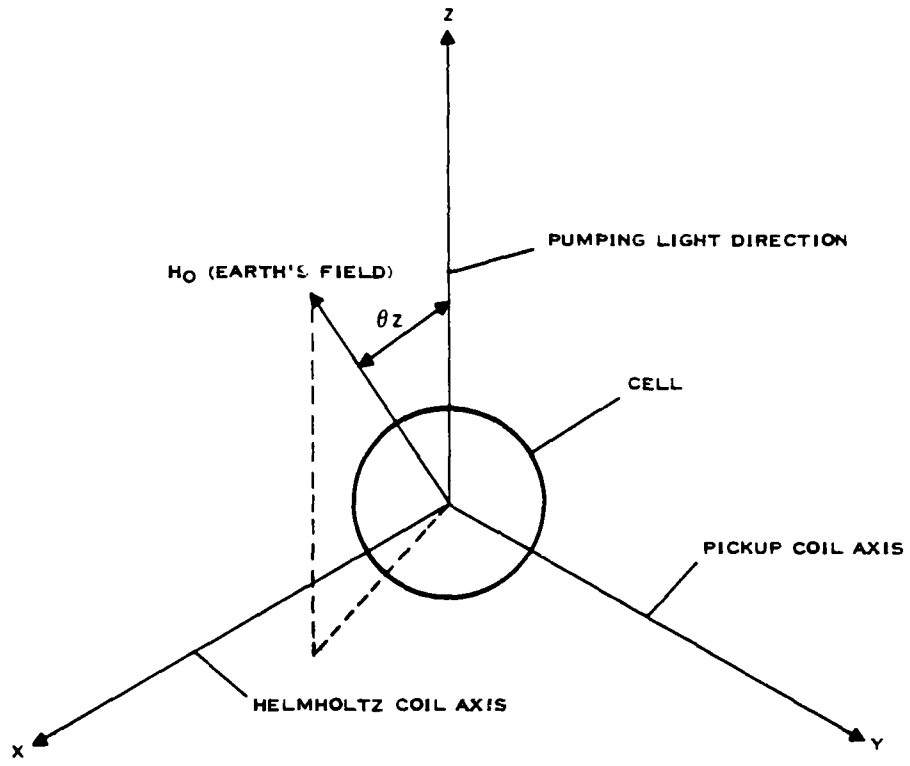


FIGURE 11. SKETCH SHOWING THE THREE AXES OF THE  
 $^3\text{He}$  FREE PRECESSION MAGNETOMETER

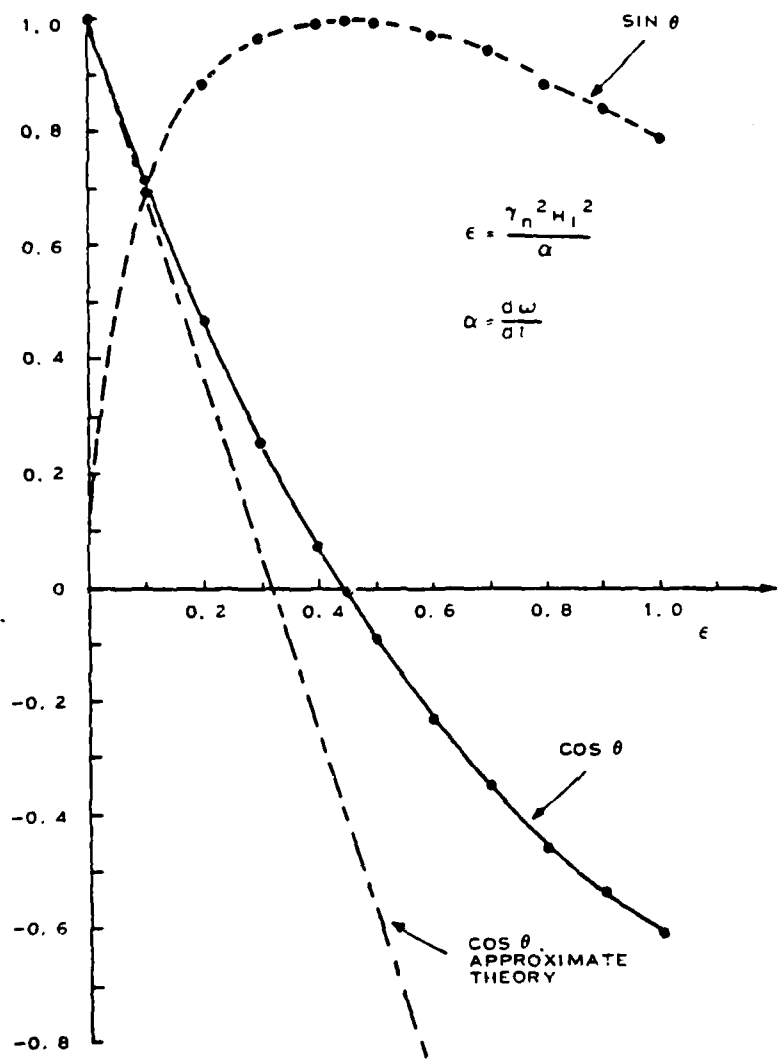


FIGURE 12. PLOT OF  $\sin \theta$  AND  $\cos \theta$  AS A FUNCTION OF THE PARAMETER  $\epsilon$ .  
 THE ANGLE  $\theta$  IS THE ANGLE BETWEEN THE CELL MOMENT AND THE  
 AMBIENT FIELD AFTER ROTATION

### 3.2 Continued

$\epsilon = \gamma_n^2 H_1^2 / \alpha$  where  $H_1$  is half the amplitude of the swept frequency magnetic field and  $\alpha$  is the sweep rate. Figure 12 is based on the assumption that  $H_1$  is perpendicular to the Earth's field  $H_0$ . For the general case in which  $H_1$  is not necessarily perpendicular to  $H_0$ , the abscissa of Figure 12 may be replaced with  $\epsilon = \gamma_n^2 H_1 \sin^2 \theta_x / \alpha$ , since only the part of  $H_1$  that is perpendicular to  $H_0$  is effective in the moment rotation. Figure 13 was prepared from Figure 12 with the modified interpretation of the abscissa. Figure 13 is a plot of the quantity  $F(\theta_x)$ , which represents the fraction of the polarization along  $H_0$  which is rotated into the precession plane. Note that multiple curves of  $F(\theta_x)$  exist, one for each choice of the magnitude of  $H_1$ . In most circumstances  $H_1$  is chosen so that a perfect moment rotation results when  $H_1$  is perpendicular to  $H_0$ . For this case the "peak  $\theta_x = 90^\circ$ " curve is appropriate. We see that  $F(\theta_x)$  is greater than 90 percent for  $\theta_x$  between 45 degrees and 90 degrees. Including the  $\cos \theta_z$  factor due to the pumping light direction, the amplitude of the precessing polarization is  $P_0 \cos \theta_z F(\theta_x)$ .

The magnetic pickup coil is sensitive only to the component of the precessing polarization that is parallel to the pickup coil axis. Since the plane of precession is perpendicular to  $H_0$ , the orientation dependence of the pickup coil is hence accounted for by a  $\sin \theta_y$  factor. Taken together the expression of the sensor pickup coil signal amplitude is

$$S = S_0 F(\theta_x) \cos \theta_z \sin \theta_y \quad (3-1)$$

where  $S_0$  is the maximum possible pickup coil signal. Equation (3-1) and (2-2) permit calculation of the dependence of the  $f^2$  part of the sensor noise from sensor orientation. We expect the low frequency part of the sensor noise to be independent of sensor orientation, although an experiment to verify this has not been performed.

As a final note to the theoretical discussion, we mention that, while no false magnetometer output (such as the light shifts in  $^4\text{He}$  magnetometers)

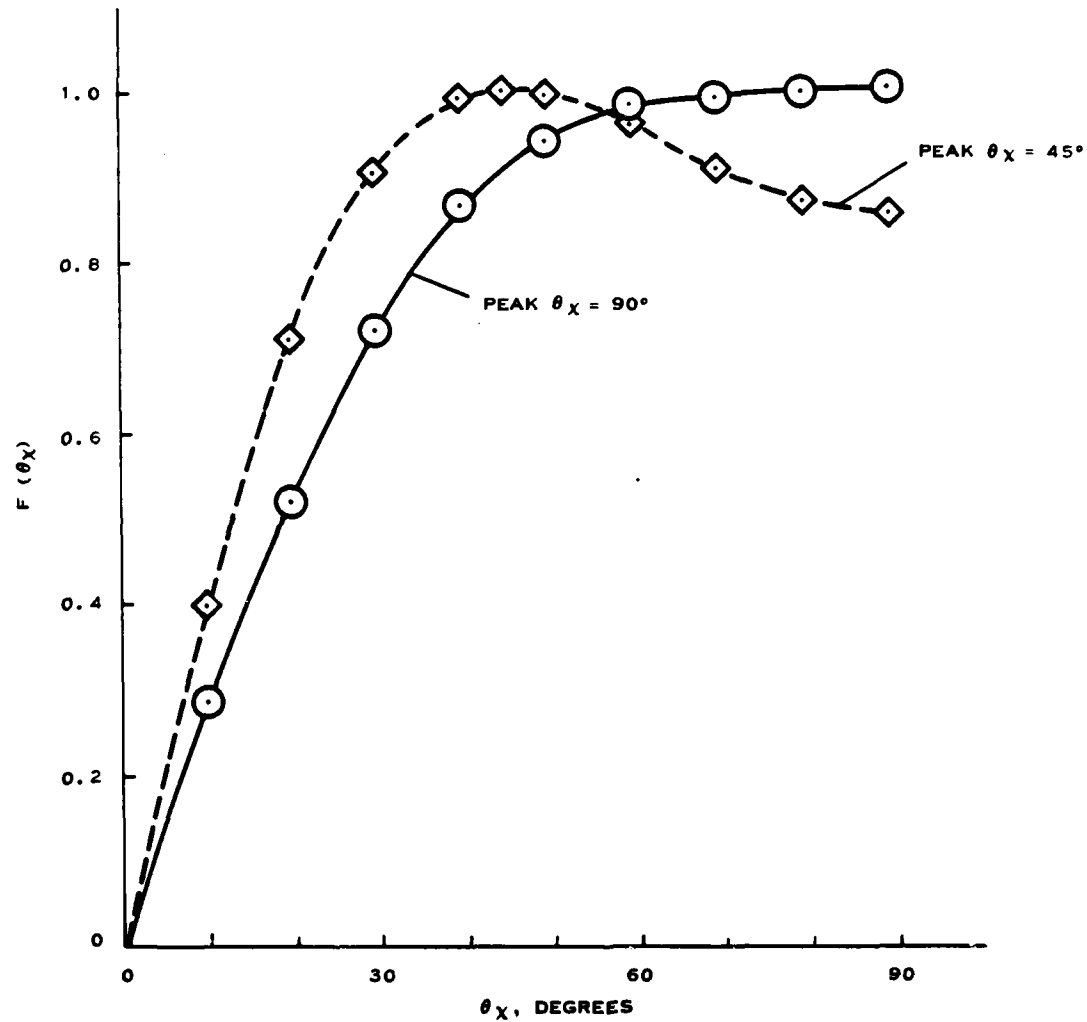


FIGURE 13. A PLOT OF THE QUANTITY  $F(\theta_X)$ , THE FRACTION OF THE POLARIZATION ALONG  $H_0$  WHICH IS ROTATED INTO THE PRECESSION PLANE, AS A FUNCTION OF  $\theta_X$ .

### 3.2 Continued

arises from a sensor rotation per se, there is a spurious magnetometer signal that is associated with the sensor rotation rate. Since the frequency of the pickup coil signal reflects the motion of the cell moment relative to the pickup coils, if the pickup coils themselves are in motion, then a spurious magnetometer signal will result. The spurious signal may be written as

$$H' = - \frac{\vec{\Omega} \cdot \vec{H}_0}{\gamma n H_0} \quad (3-2)$$

where  $\vec{\Omega}$  is the rotation rate of the sensor. In a rigid gradiometer, both sensors experience the same  $\vec{\Omega}$  and so the rotation signal disappears.

### 3.3 Experimental Results

Figures 14 and 15 exhibit the results of an experiment to demonstrate the XDM magnetometer's orientation dependence. The conditions for Figure 14 were such that the Helmholtz coil axis (the x axis of Figure 11) was directed along an east-west line. The abscissa of Figure 14 is the direction of the pumping light relative to the vertical with the sensor being rotated about the Helmholtz coil axis. At the Sherman, Texas magnetic test site, the dip angle is 63 degrees, so the peak signal occurs with the light beam 27 degrees from the vertical. A rough agreement between the experimental values and the theory of equation (3-1) is apparent. The difference between experiment and theory may be attributed to nonparallel pumping light and changes in pumping light intensity due to cable movements that occurred when the sensor was rotated.

In the experiment of Figure 15 the Helmholtz coil axis was aligned in the north-south direction. The signal level as the sensor was rotated about the Helmholtz coil axis is plotted as a function of the light direction. The agreement of theory with experiment is adequate.

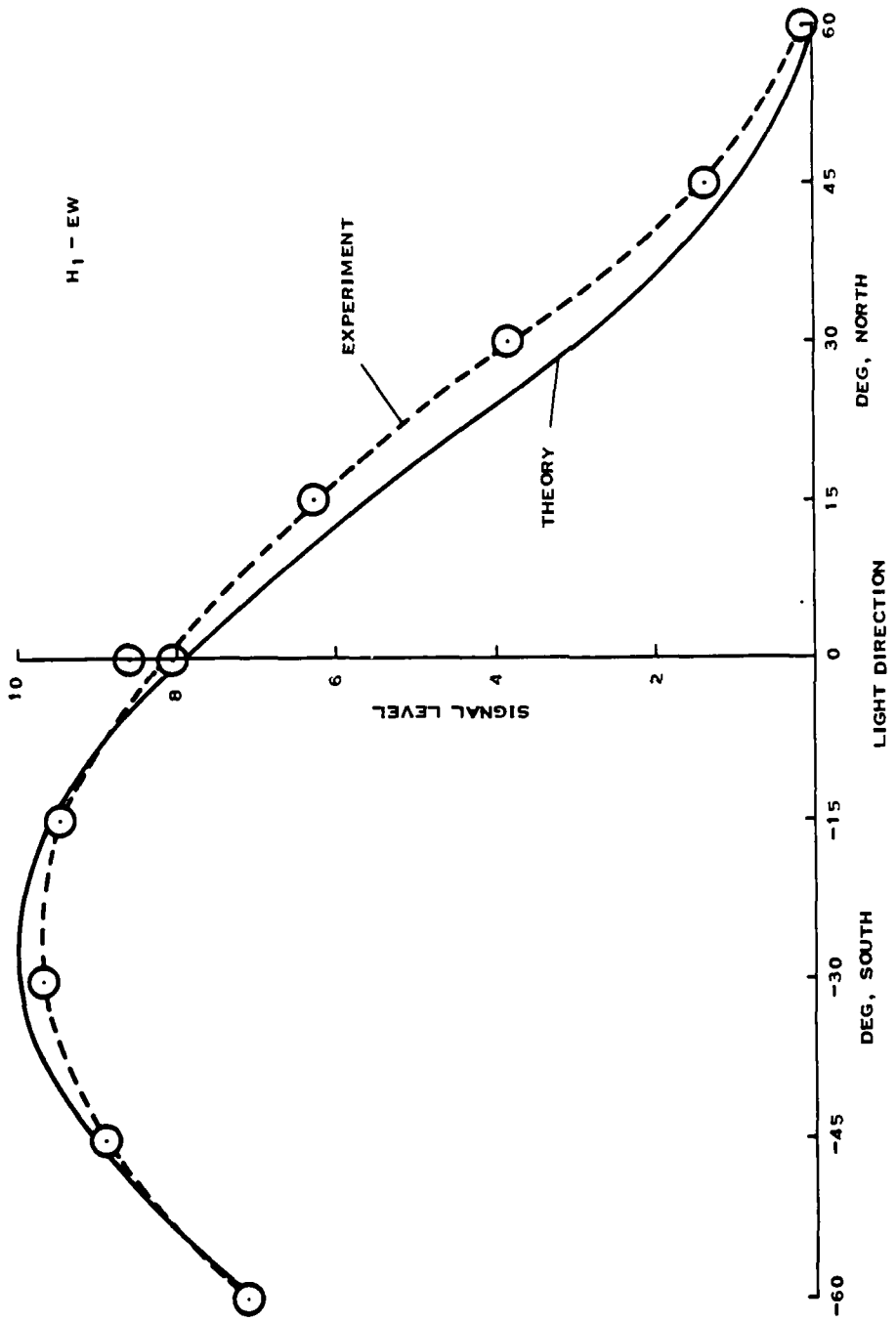


FIGURE 14. PLOT OF SIGNAL AMPLITUDE FROM SENSOR PICKUP COILS AS A FUNCTION OF PUMPING LIGHT DIRECTION RELATIVE TO THE VERTICAL. THE SENSOR WAS ROTATED ABOUT THE HELMHOLTZ COIL AXIS, WHICH WAS DIRECTED ALONG AN EAST-WEST LINE

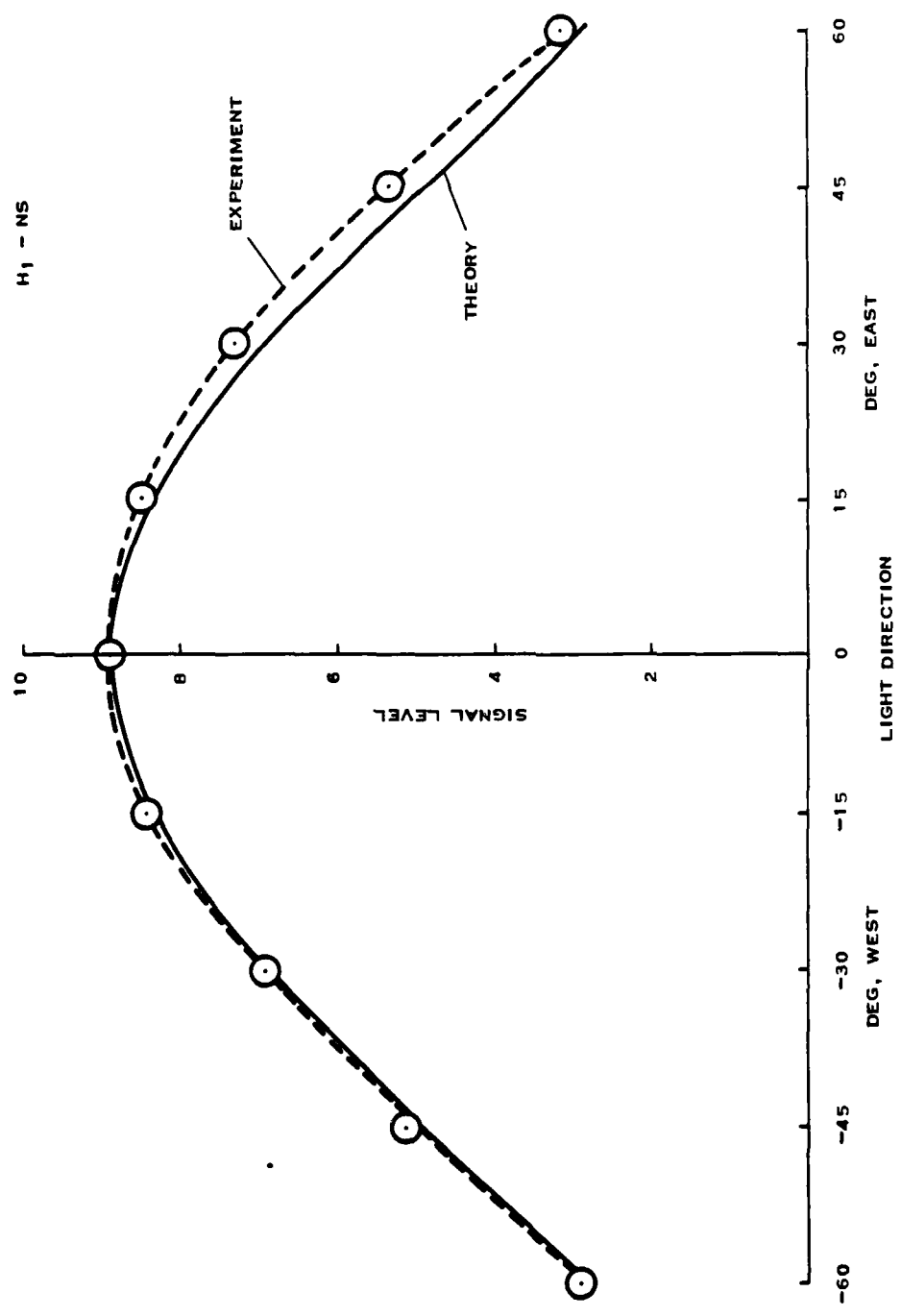


FIGURE 15. PLOT OF SIGNAL AMPLITUDE FROM SENSOR PICKUP COILS AS A FUNCTION OF PUMPING LIGHT DIRECTION RELATIVE TO THE VERTICAL. THE SENSOR WAS ROTATED ABOUT THE HELMHOLTZ COIL AXIS, WHICH WAS DIRECTED ALONG AN EAST-WEST LINE.

## SECTION 4

### EFFECT OF MAGNETIC MOMENT PROXIMITY

#### 4.1 INTRODUCTION

If a magnetic moment is brought near to a  $^3\text{He}$  magnetometer, it is observed that the free precession relaxation time is reduced. An analysis shows that the magnetic field gradient at the cell position due to the magnetic moment is responsible for the decreased  $T_2$ . In this section we present the results of the theory of gradient relaxation and an experimental determination of the gradient relaxation rate.

#### 4.2 Theory of Gradient Relaxation

We consider a collection of  $^3\text{He}$  atoms experiencing random motion within a cell of length  $L$  along the  $x$  axis. Due to the presence of a magnetic gradient each atom (with position coordinates  $x, y, z$ ) sees a time-varying field with components

$$H_z(t) = H_0 + \frac{\partial H_z}{\partial x} x(t) \quad (4-1)$$

$$H_x(t) = \frac{\partial H_x}{\partial x} x(t) \quad (4-2)$$

$$H_y(t) = \frac{\partial H_y}{\partial x} x(t) \quad (4-3)$$

For simplicity we have assumed that only gradients in the  $x$  direction exist. In equation (4-1)  $H_z$  is the magnetic field at the center of the cell (at  $x=0$ ) and the  $z$  direction is taken as the direction of  $H_0$  (which is assumed perpendicular to the  $x$  axis). The small time-varying field that the atoms experience as they move about in the cell is sufficient to rotate some of them out of the plane of precession. According to Slichter<sup>3</sup> the transverse relaxation rate due to magnetic gradients is given by

4.2 Continued

$$\frac{1}{T_{2\bar{V}H}} = \frac{1}{2} \gamma_n^2 S_{Hz}(0) \quad (4-4)$$

where  $S_{Hz}(\omega)$  is the spectrum of the random variable  $H_z(t)$ .

We have not included in equation (4-4) a term proportional to  $S_{Hy}(\omega_0)$  (where  $\omega_0 = \gamma_n H_0$ ) which, upon evaluation, turns out to be insignificant. The spectrum  $S_{Hz}(\omega)$  is by definition

$$S_{Hz}(\omega) = \int_{-\infty}^{\infty} E \{ H_z'(t) H_z'(t + \tau) \} e^{-i\omega\tau} d\tau \quad (4-5)$$

$$= \left( \frac{\partial H_z}{\partial x} \right)^2 \int_{-\infty}^{\infty} E \{ x(t) x(t + \tau) \} e^{-i\omega\tau} d\tau \quad (4-6)$$

In equations (4-5) and (4-6)  $E$  represents the expectation operator, and  $H_z'(t)$  is simply  $H_z(t)$  with the mean (i.e.,  $H_0$ ) removed. The technique described by Papoulis<sup>4</sup> has been used to find an approximate value for  $E\{x(t)x(t + \tau)\}$  for atoms confined between two plane surfaces (at  $\pm L/2$ ). The result is

$$R_x(\tau) = E\{x(t)x(t + \tau)\} = \frac{L^2}{12} e^{-\frac{10D|\tau|}{L^2}} \quad (4-7)$$

where  $D$  is the diffusion coefficient of the helium gas. From equations (4-4), (4-6), and (4-7) we find that<sup>2</sup>

$$\frac{1}{T_{2\bar{V}H}} = \frac{\gamma_n^2 L^4 (\partial H_z / \partial x)^2}{120D} \quad (4-8)$$

For  ${}^3\text{He}$  at 10 torr pressure and  $300^\circ\text{K}$ ,  $D$  is<sup>5</sup>  $136.5 \text{ cm}^2/\text{sec}$ .

#### 4.2 Continued

Equation (4-8) gives the gradient relaxation rate which is appropriate for cylindrical cells with the gradient along the cell axis. We next turn our attention to spherically shaped cells. We note that, for a cylindrical cell,  $E(x^2)$  takes the value  $L^2/12$ . For a sphere of radius  $R$ ,  $E(x^2)$  is  $R^2/5$ . An approximate expression for the gradient relaxation rate is then found by replacing  $L^4$  of equation (4-8) with  $(12R^2/5)^2$ :

$$\frac{1}{T_{2VH}} = \frac{6 \gamma_n^2 R^4 (\partial H_z / \partial x)^2}{125D} \quad (4-9)$$

#### 4.3 Experimental Results

The gradient was produced with two 10 turn 3.25 inch diameter coils arranged as shown in Figure 16. The coil axes were aligned with the Earth's field and the coil centers were positioned along an east-west line. With opposing current directions for the two coils, a pure gradient is produced at the sensor position. The measured free precession time  $T_{2VH}$  due to gradient relaxation (with the natural cell relaxation time removed) is exhibited in Figure 17. The abscissa is the gradient  $\partial H_z / \partial x$ . The upper plot (the 2 inch diameter spherical cell) characterizes the gradient sensitivity of the XDM  $^3\text{He}$  free precession magnetometer. The lower plot (for the 5 inch long cylindrical cell) presents the results of an experiment performed with an earlier sensor before the XDM contract period. The plot is included for completeness. Both curves agree well with theory. The agreement is particularly important in lending confidence to equation (4-9), which is approximate. The considerable reduction in gradient sensitivity of the 2 inch spherical cell from that of the 5 inch cylindrical cell is apparent.

For one electric current setting, the coils of Figure 16 were aligned along the  $y$  axis (i.e., perpendicular to  $H_0$ ). For this case the gradient  $\partial H_y / \partial x$  was about 0.9 gamma/cm. As indicated in Figure 17 the relaxation rate due to  $\partial H_y / \partial x$  is much less than that due to an equal magnitude of  $\partial H_z / \partial x$ . The relative insensitivity of the  $T_2$  relaxation rate to  $\partial H_y / \partial x$  is predicted by theory.

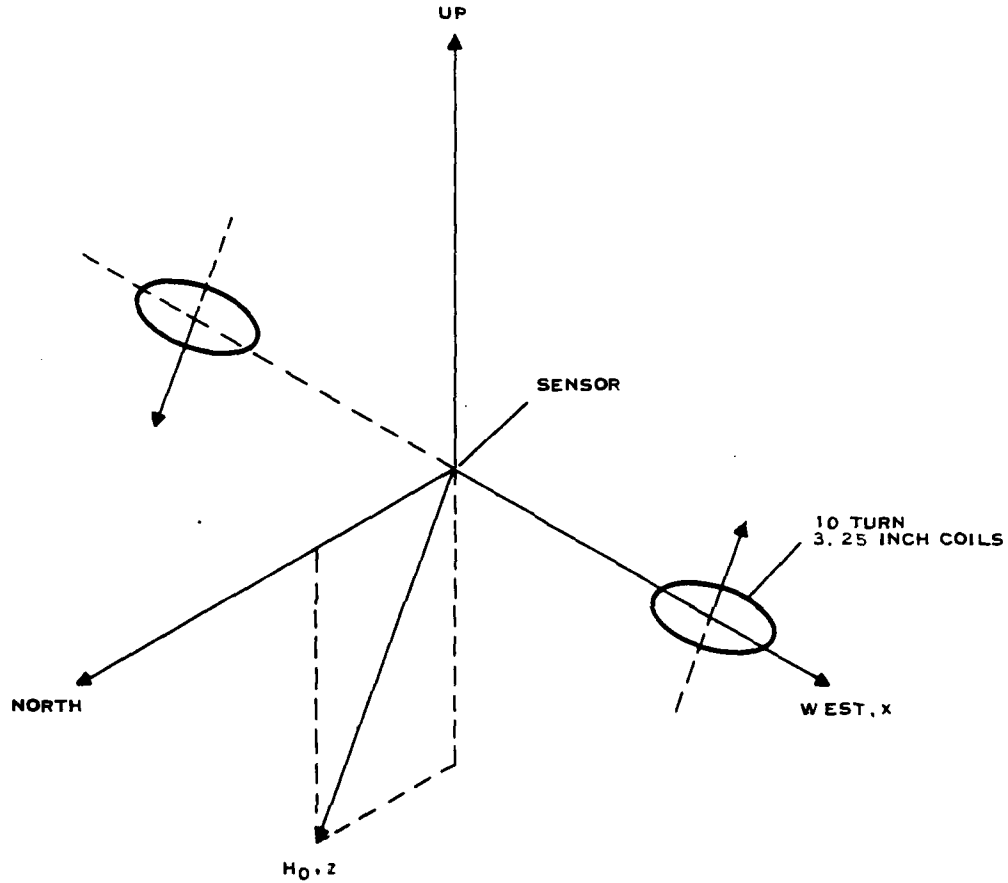


FIGURE 16. SKETCH SHOWING PLACEMENT OF  $^3\text{He}$  FREE PRECESSION SENSOR AND MAGNETIC GRADIENT PRODUCING COILS. THE COILS ARE LOCATED 3 FEET FROM THE SENSOR AND ARE ORIENTED WITH THEIR AXES EITHER PARALLEL WITH THE EARTH'S FIELD (ALONG THE  $z$  AXIS) OR PERPENDICULAR TO THE EARTH'S FIELD (ALONG THE  $y$  AXIS).

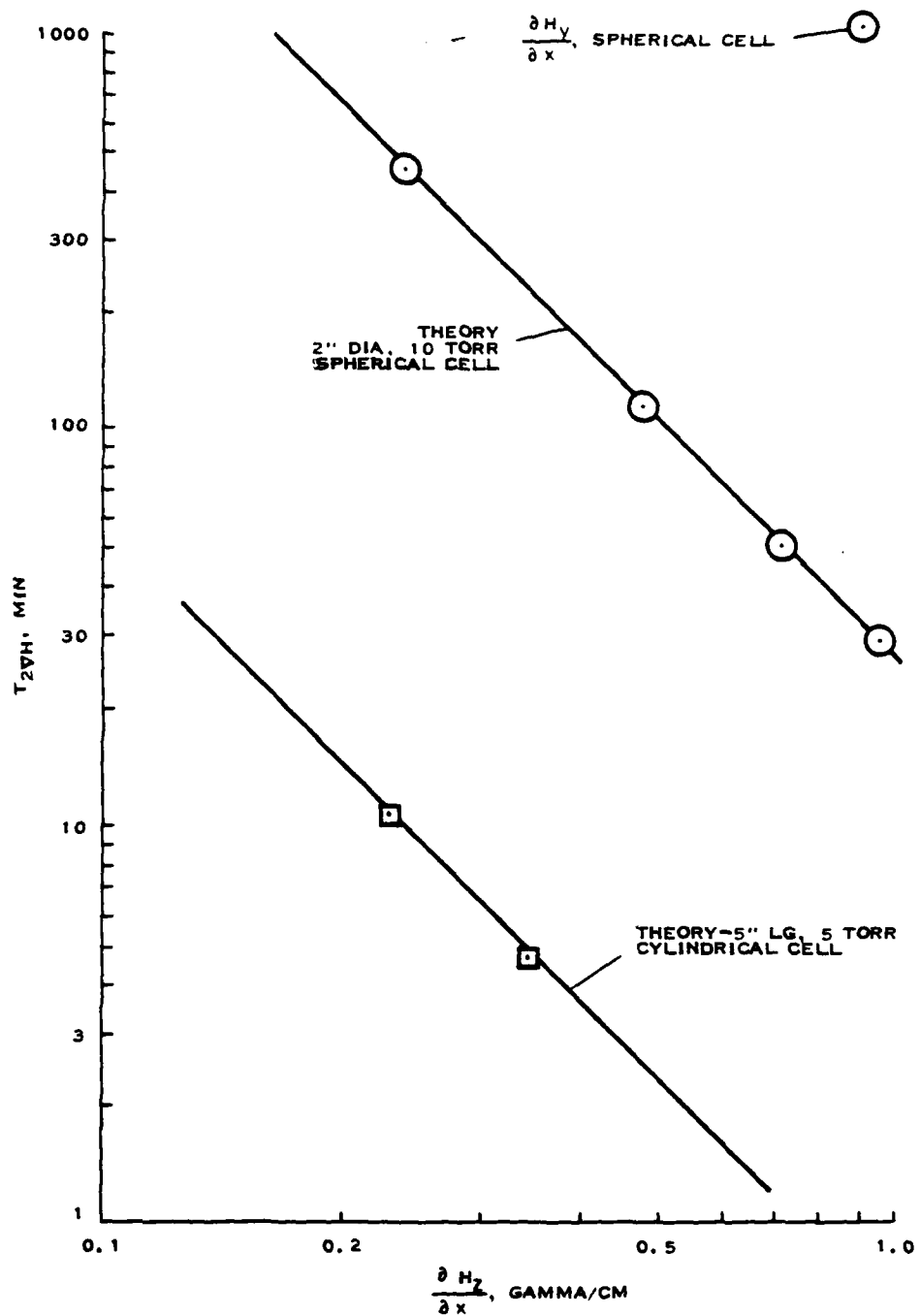


FIGURE 17. THE FREE PRECESSION RELAXATION TIME  $T_{2\Delta H}$  VERSUS THE MAGNETIC GRADIENT  $\frac{\partial H_z}{\partial x}$ . THE NATURAL RELAXATION TIME HAS BEEN REMOVED FROM THE EXPERIMENTAL POINTS (MARKED AS CIRCLES AND SQUARES)

## SECTION 5

### MOVING DIPOLE DETECTION TEST

#### 5.1 Introduction

An application of particular importance for the XDM  $^3\text{He}$  gradiometer is its use in the detection of a magnetic target. In order to demonstrate the detection ability of the XDM  $^3\text{He}$  gradiometer in a direct fashion, an experiment was devised in which a magnetic dipole was carried past the gradiometer. The experiment was similar to the detection test reported in an earlier contract effort<sup>1</sup> except that the magnet path was 150 feet from the gradiometer as compared with 100 feet in Reference 1. The specifics of the detection test are first described in this section, then the results of signal processing of the gradiometer signal record are presented.

#### 5.2 Detection Test

The equipment block diagram for the test is shown in Figure 18. The analog output of the frequency discriminator was directed through an A/D converter into the HP 9835 computer, which stored the (unfiltered) data in its memory. After 6000 sec of data (at a 1 Hz rate) were accumulated in the 9835 memory, the data were recorded on a magnetic tape cartridge. A total of about 15000 sec of data (including gradiometer noise and six magnet signals) was recorded. The digital signal analyzer of Figure 18 permitted noise spectra to be made during data storage. The signal processing portion of the experiment involved reloading the magnetic tape record into the HP 9835 memory, filtering the string of data with a digital bandpass filter, and passing the result through a D/A converter into the chart recorder which exhibited the filtered signal. Processed data were also printed on a paper tape using the built-in printer of the HP 9835 computer.

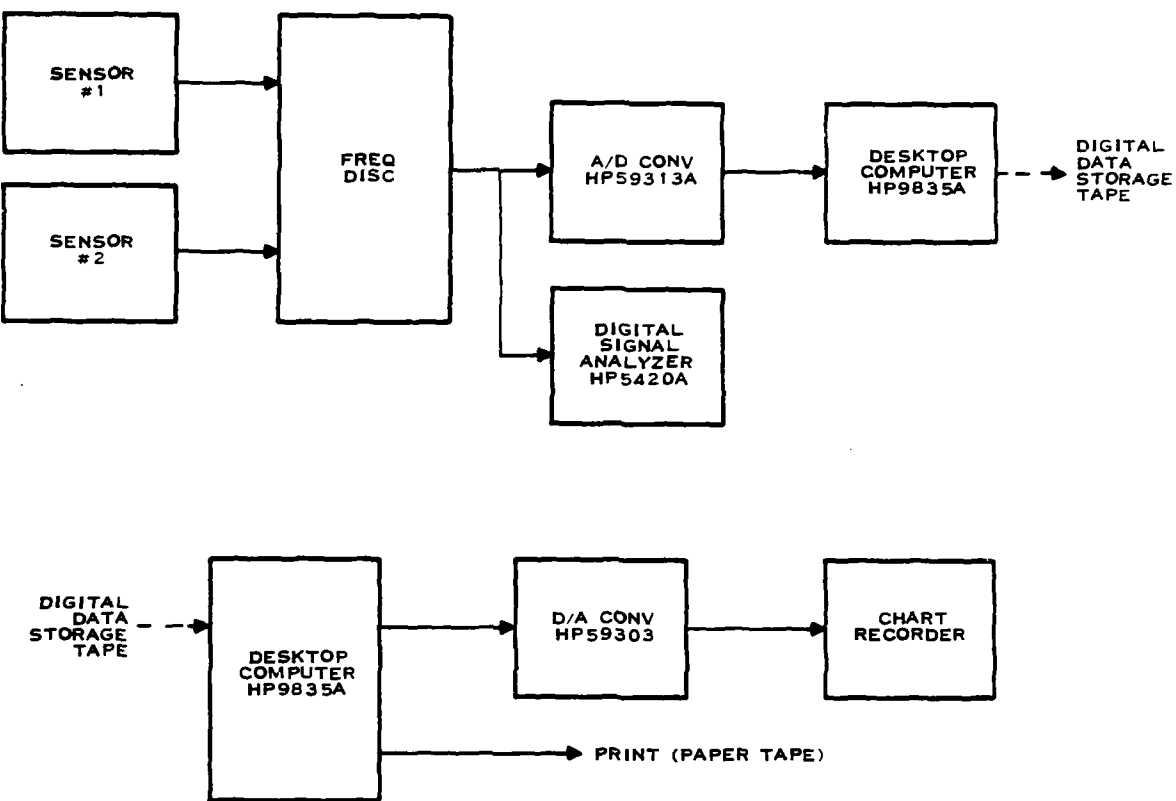


FIGURE 18. BLOCK DIAGRAM FOR MOVING DIPOLE DETECTION TEST

## 5.2 Continued

Figure 19 is a map showing the magnet path for the moving dipole test. A bar magnet of moment  $m = 3.4 \times 10^5 \text{ gamma-ft}^3 = 0.96 \times 10^5 \text{ G-cm}^3$  was aligned with the Earth's field direction and was carried along a path 150 feet from the gradiometer. The path was in the magnetic north direction. The magnet was carried at 7.5 ft/sec (4.44 knot) toward the north. The  $^3\text{He}$  magnetometers were separated by 13.33 feet in the east-west direction.

A plot of the noise free theoretical gradiometer signal is provided in Figure 20. The signal is a maximum at closest approach, where it takes the value 26.8 milligamma. The duration of the signal, defined as the time interval between points of half maximum, is 19 seconds.

For the detection test the sensors were oriented with the pumping light in the vertical direction. Just after pumping (at 1:04 PM) on the day of the test, the gradiometer signal-to-noise parameter was 41.75 dB-Hz. At 5:45 PM the gradiometer signal-to-noise parameter was 39.36 dB-Hz. A gradiometer noise spectrum taken at 4:40 PM during a portion of the test with no target signal is shown in Figure 21. The natural frequency of the phase locked loops of the frequency discriminator was 0.1 Hz.

## 5.3 Processing of Gradiometer Signal

Two digital bandpass filters were implemented on the HP 9835 computer. The unfiltered data from the frequency discriminator were passed through each filter in a separate operation (i.e., the filters were not cascaded).

The transfer functions of the filters appear in Figure 22. Each filter was constructed through use of a bilateral transform of a 6 pole Bessel low pass filter.

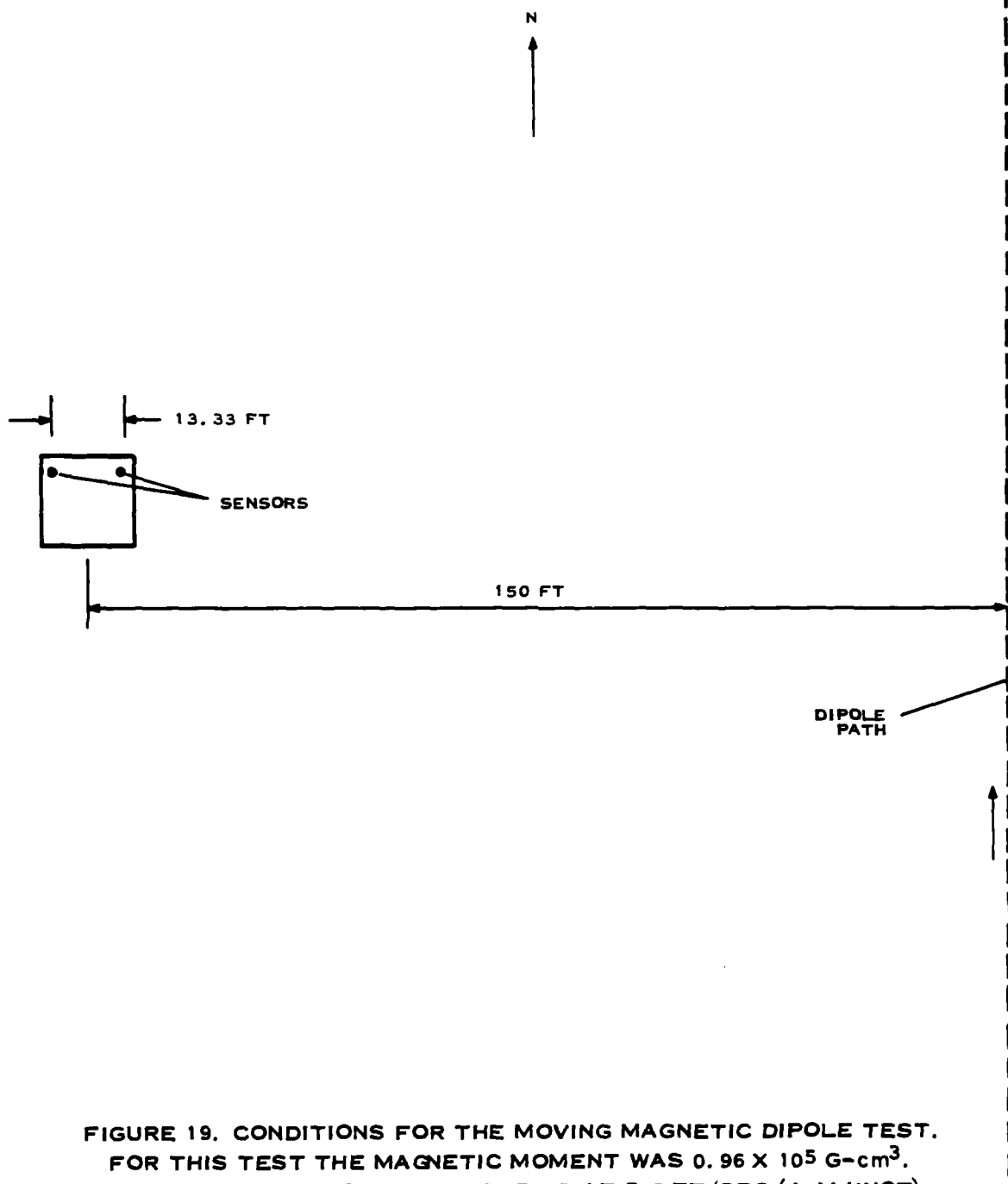


FIGURE 19. CONDITIONS FOR THE MOVING MAGNETIC DIPOLE TEST.  
 FOR THIS TEST THE MAGNETIC MOMENT WAS  $0.96 \times 10^5$  G-cm<sup>3</sup>.  
 THE MAGNETIC DIPOLE WAS CARRIED AT 7.5 FT/SEC (4.44 KNOT).

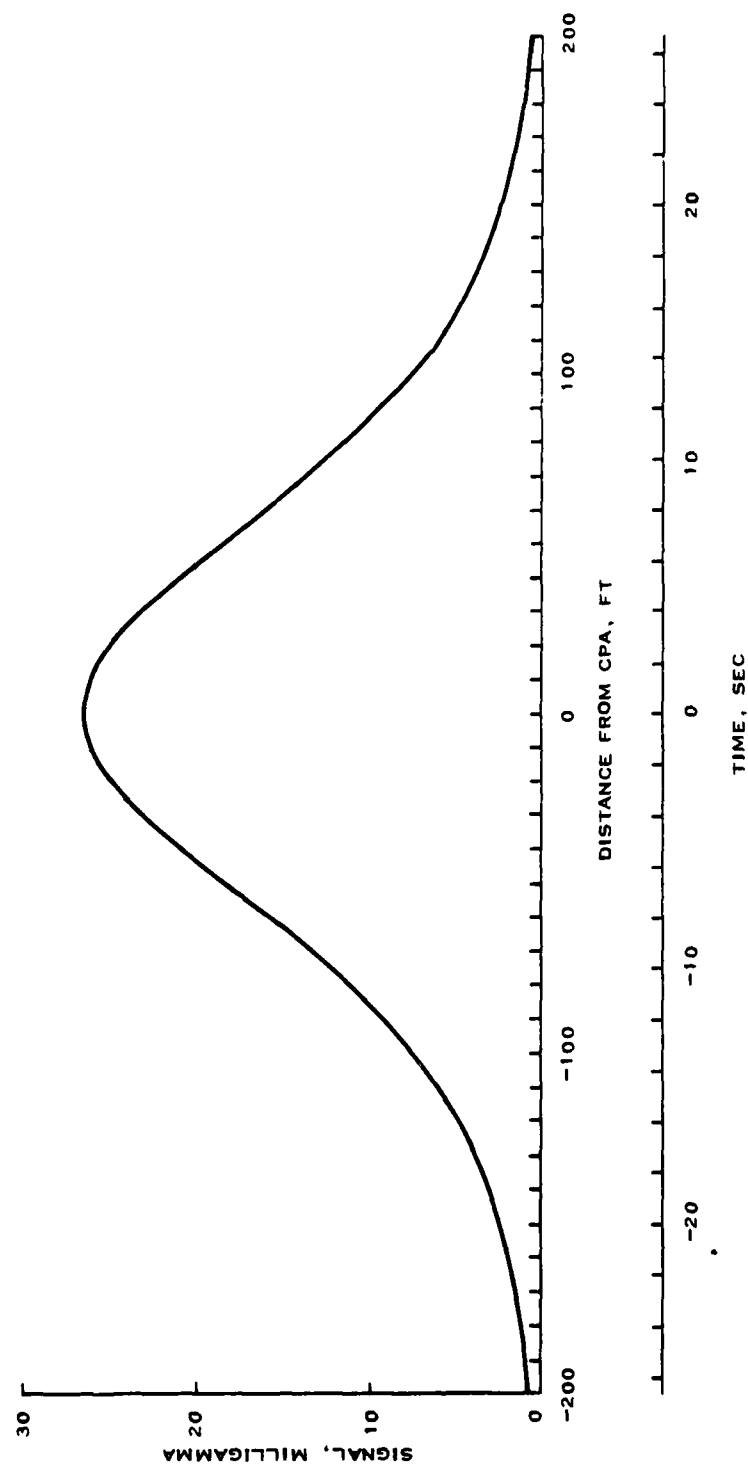


FIGURE 20. PLOT OF THEORETICAL GRADIOMETER SIGNAL AS A FUNCTION  
OF DISTANCE ALONG PATH (AND TIME)

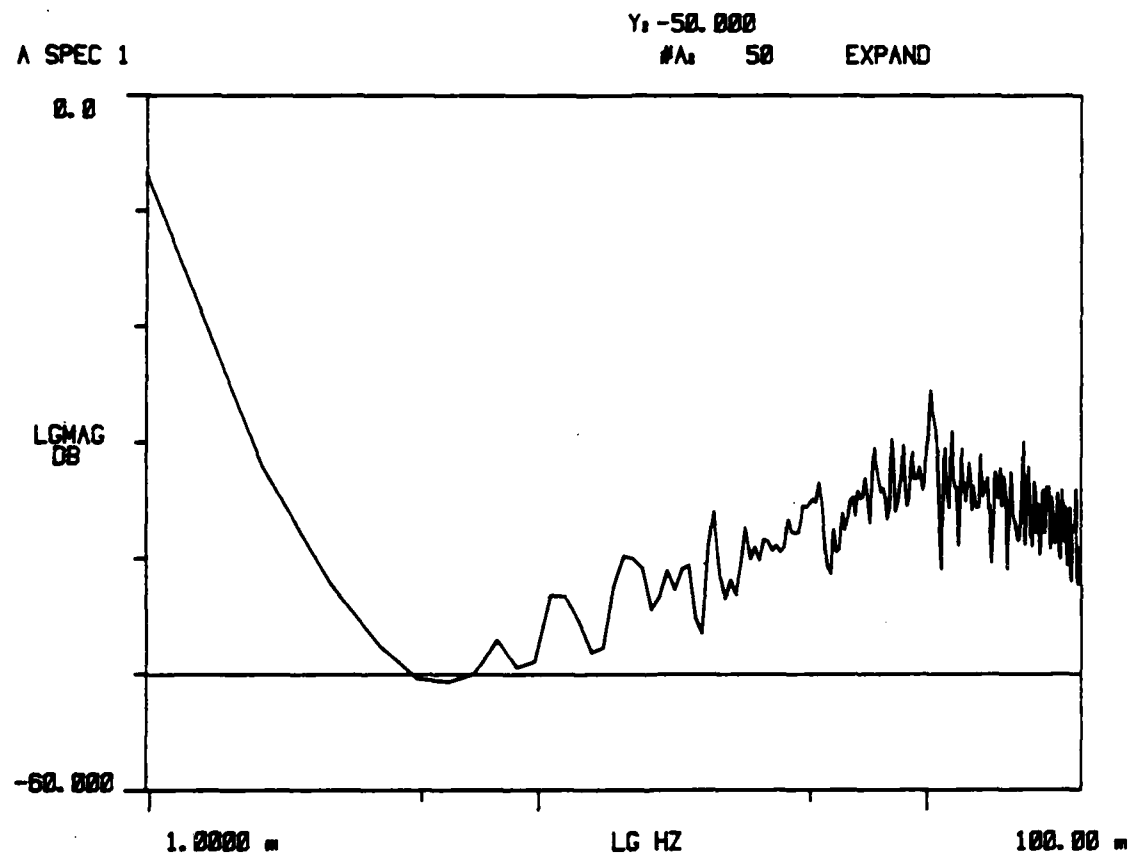


FIGURE 21. SPECTRUM OF XDM  $^3\text{He}$  GRADIOMETER NOISE TAKEN DURING DETECTION TEST. NO TARGET SIGNAL WAS PRESENT DURING SPECTRUM TIME INTERVAL. 0 dB = 1 GAMMA  $^2/\text{HZ}$ . THE SENSORS WERE ORIENTED FOR VERTICAL PUMPING

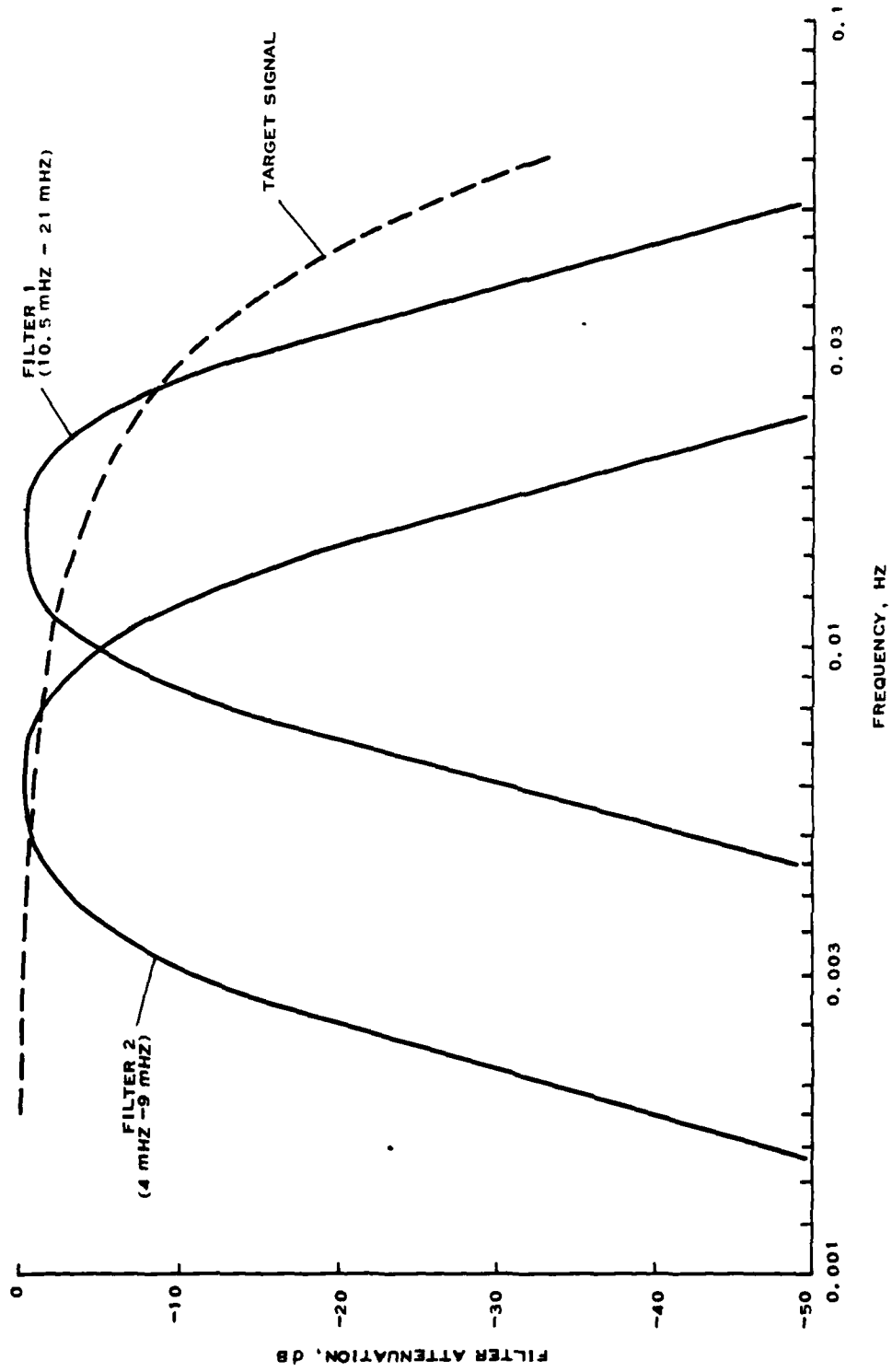


FIGURE 22. TRANSFER FUNCTIONS OF THE DIGITAL BANDPASS FILTERS USED IN PROCESSING OF  
GRADIOMETER SIGNAL

### 5.3 Continued

Filter 1, with 3 dB points at 10.5 and 21 mHz, was chosen to pass the target spectrum (see Figure 22) and reject the low frequency noise. The characteristics of Filter 2 were selected to pass the frequency interval containing the least noise (see Figure 21). The bandpass 3 dB points occur at 4 and 9 mHz.

A record of the output of filter 1 showing the target signal is given in Figure 23. The oscillatory response of the bandpass filter to the target signal of Figure 20 is apparent. The maximum signal associated with the magnet walkby in 9.28 milligamma; this value represents 35 percent of the target signal of 26.8 milligamma. Since the RMS noise level through the filter was measured to be 1.11 milligamma, the signal-to-noise ratio is an easily detectable 8.38. The signal maximum occurs 102 seconds after time of closest approach. An earlier signal peak (with  $S/N = 7.72$ ) is observed at 72 seconds after time of closest approach. It might be noted in parenthesis that the time delay associated with the bandpass filters was anticipated. While the time delay problem was not addressed in the present effort, techniques to reduce the delay are known to exist. A 15 minute interval of gradiometer noise passed through Filter 1 is given in Figure 24.

A time record of the output of Filter 2 which includes the target event is presented in Figure 25. The same portion of unfiltered gradiometer signal record was used for both Figures 23 and 25. Because the bandpass of Filter 2 is less than Filter 1, the signal maximum due to the target has been reduced to 5.71 milligamma (from 9.28 milligamma) or 21 percent of the unfiltered signal. The RMS noise has also been reduced from 1.11 to 0.418 milligamma, resulting in a signal-to-noise ratio of 13.7. The signal maximum covers 158 seconds after time of closest approach. A 30 minute interval of filtered gradiometer noise is given in Figure 26.

An important characteristic of the (filtered) gradiometer noise involves the number of times that the noise signal crosses a given threshold. Figure 27 is a plot of the false alarm rate (the rate of threshold crossings) as a function

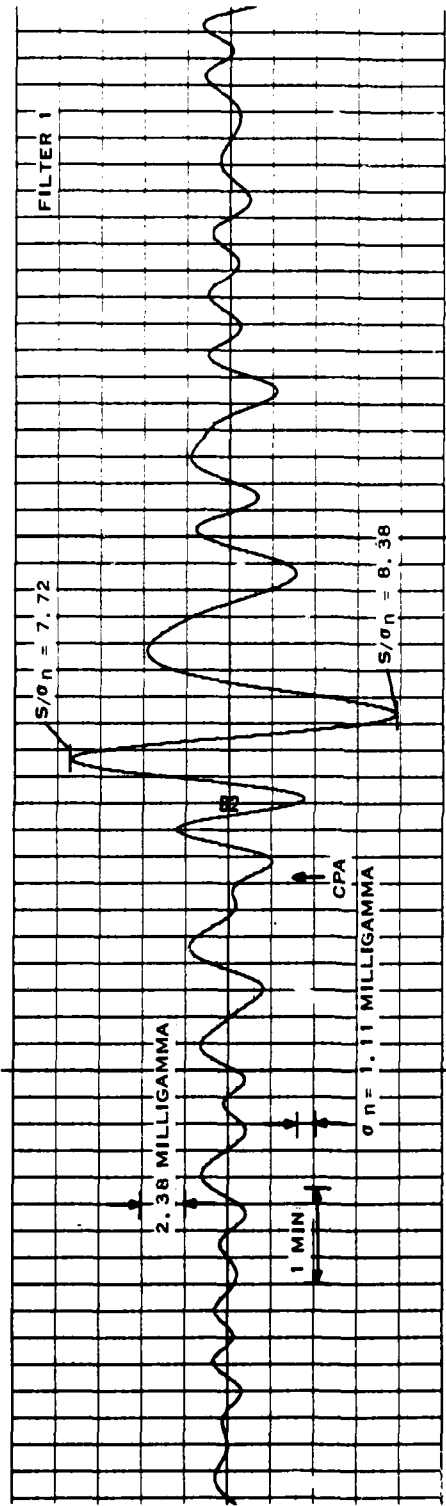


FIGURE 23. CHART RECORDING OF RADIOMETER SIGNAL PASSED THROUGH FILTER 1. THE TIME CORRESPONDING TO THE POINT OF CLOSEST APPROACH OF MAGNET TO RADIOMETER IS MARKED CPA

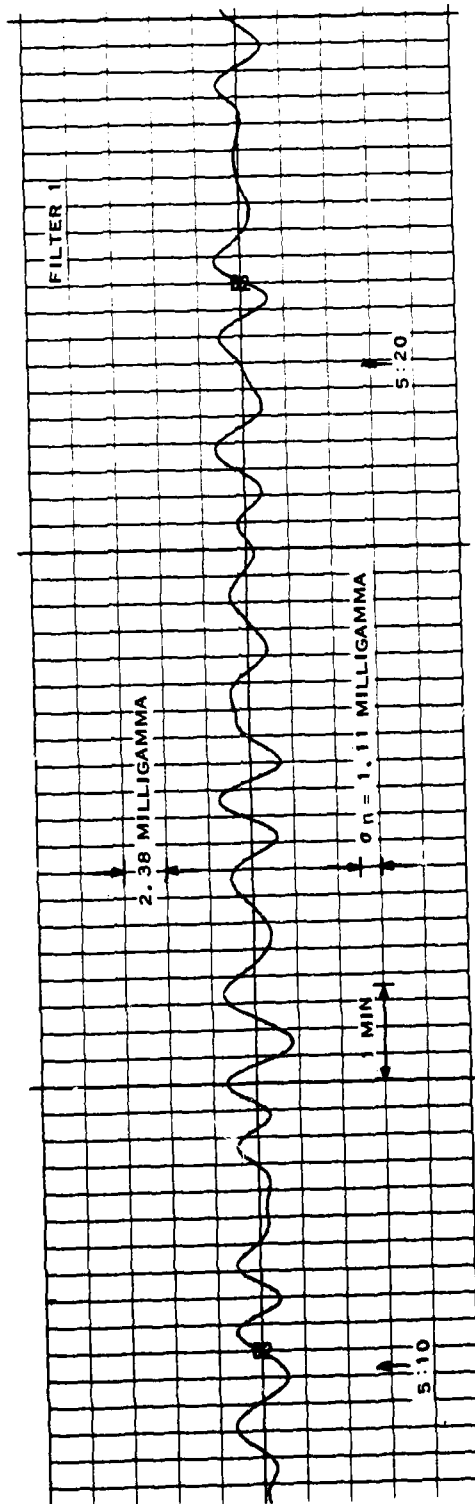


FIGURE 24. CHART RECORDING OF GRADIOMETER NOISE PASSED THROUGH FILTER 1.

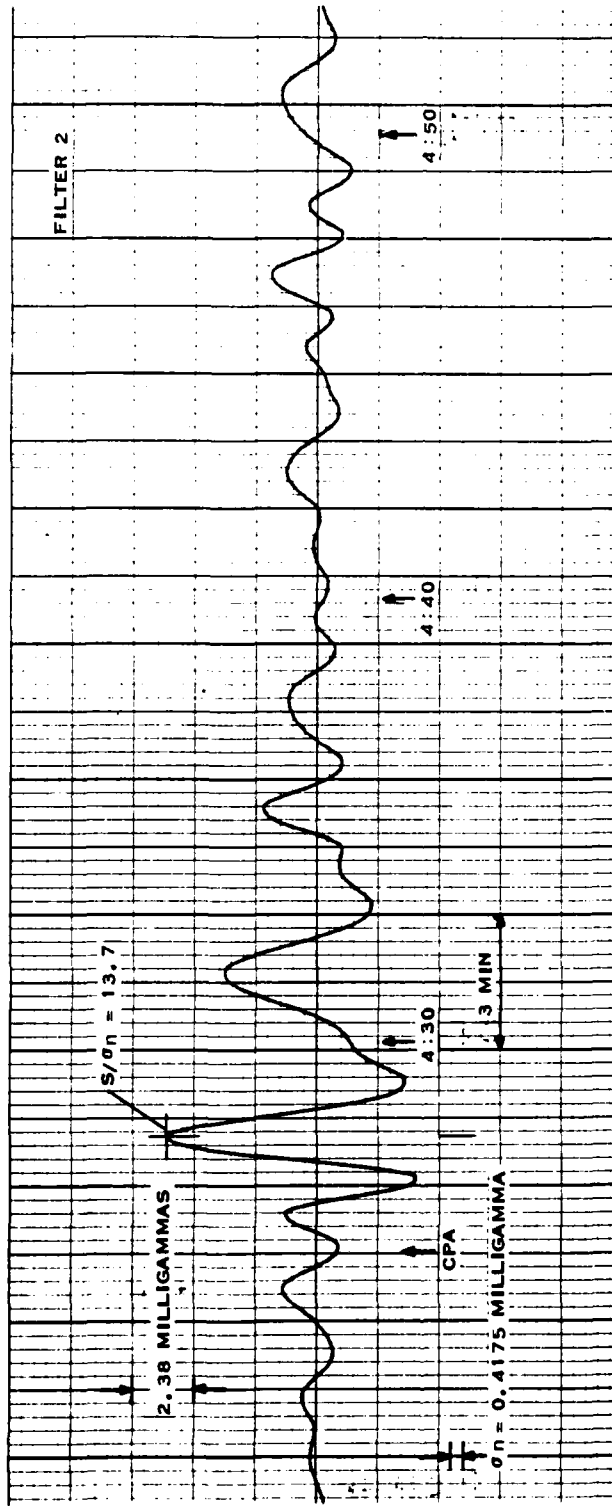


FIGURE 25. CHART RECORDING OF GRADIOMETER SIGNAL PASSED THROUGH FILTER 2

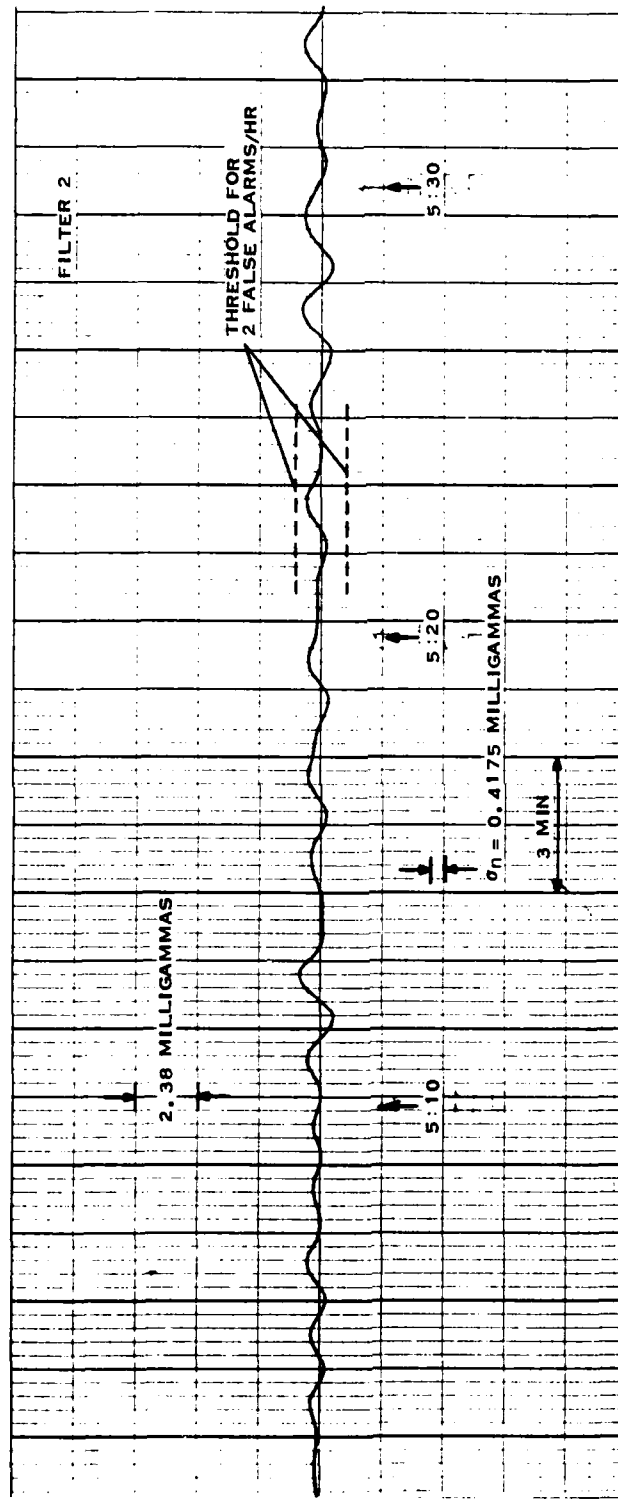


FIGURE 26. CHART RECORDING OF GRADIOMETER NOISE PASSED THROUGH FILTER 2

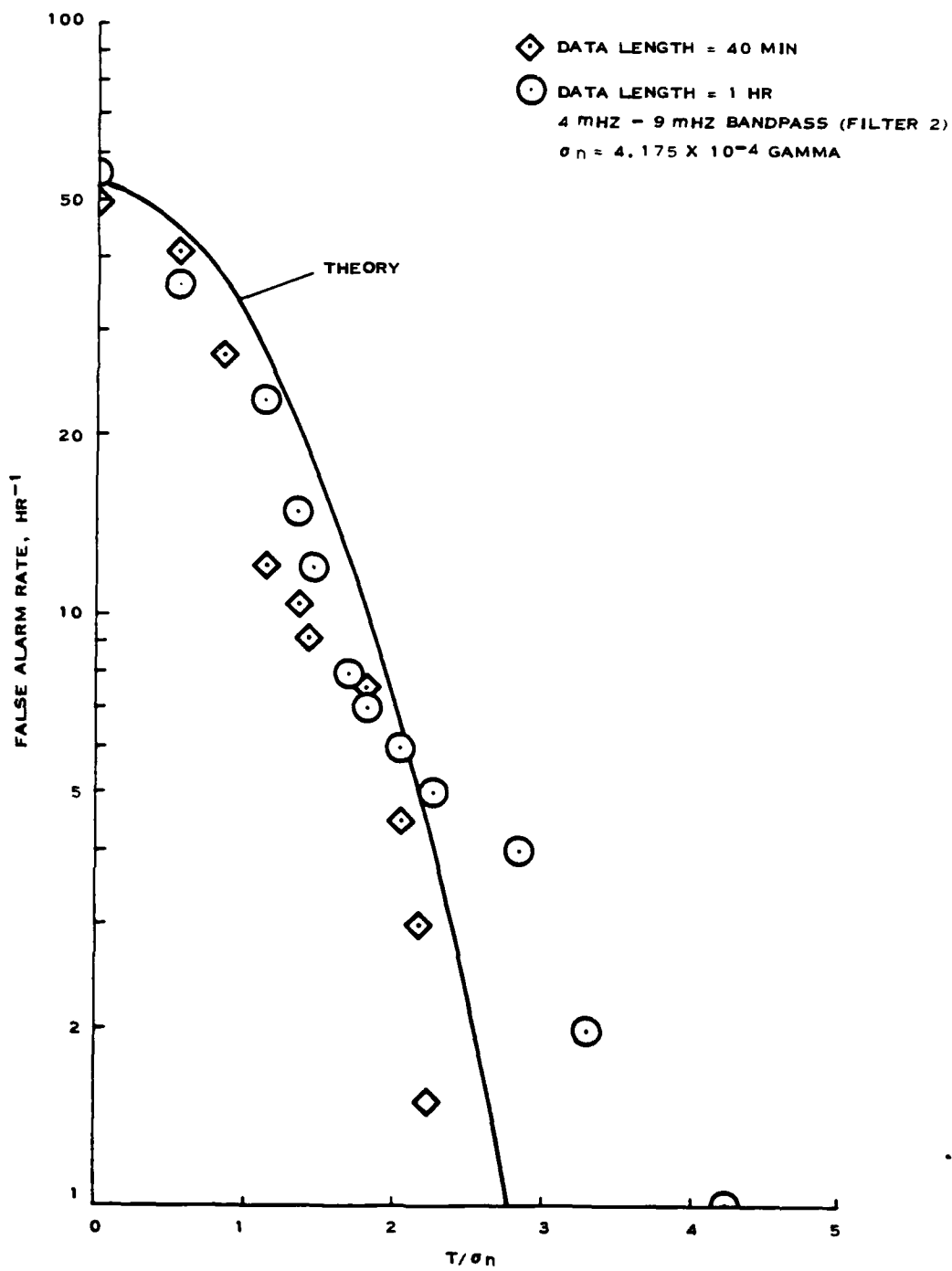


FIGURE 27. PLOT OF FALSE ALARM RATE AS A FUNCTION OF THRESHOLD SETTING. THE SQUARES AND CIRCLES DENOTE EXPERIMENTAL POINTS.

### 5.3 Continued

of the ratio  $T/\sigma_n$  where  $T$  is the threshold setting and  $\sigma_n$  is the RMS noise level. Figure 27 was prepared using gradiometer noise passed through Filter 2. An example of a threshold setting of  $T/\sigma_n = 2.56$  is indicated in Figure 26. The experimental points of Figure 27 were obtained by counting the number of threshold crossings for various threshold settings. The theoretical curve was calculated from an expression derived using the assumption of gaussian noise. The rough agreement between the experimental points and the theory suggests that the noise is indeed approximately gaussian. The analysis of Appendix B also supports this conclusion. From Figure 27 we see that the threshold setting shown in Figure 26 (for  $T/\sigma_n = 2.56$ ) corresponds to false alarm rate of 2 per hour. Since the target signal-to-noise ratio is 13.7, we may be confident that, for the threshold setting of  $T/\sigma_n = 2.56$ , essentially all targets will be detected (i.e., a near unity probability of detection).

The results of a more advanced signal processing technique than that of this section are presented in Appendix B. In this appendix the quadratic signal  $\epsilon(t)$  is introduced, where  $\epsilon(t)$  is defined by

$$\epsilon(t) = \int_0^{\Delta t} y^2(t-\tau) d\tau \quad (5-1)$$

The quantity  $y(t)$  is the bandpass filtered gradiometer signal and  $\Delta t$  is a suitably chosen time interval. When  $\epsilon(t)$  passes above a selected threshold, a detection is identified. The general statistical theory of the approach and the application of the theory to the  $^3\text{He}$  gradiometer is given in Appendix B.

## SECTION 6 SUMMARY

The following statements summarize the more important results of the present contract effort:

1. A XDM  $^3\text{He}$  gradiometer has been built and tested.
2. Each  $^3\text{He}$  sensor contains a 2 inch diameter spherical 1723 aluminosilicate cell (with average  $T_2 = 16$  hours) which is pumped for 320 seconds by two opposing lamps. The sensor occupies a volume 5 inch in diameter, 3.5 inch long.
3. The gradiometer electronics provide for automatic pumping of the cell, moment rotation, and lock-in of the frequency discriminator.
4. The amplitude of the signal from the pickup coils of the sensor is dependent upon the sensor orientation. Experiments have verified a theoretical expression of this dependence and demonstrated that a vertically oriented sensor (at the Sherman, Texas test site) has a pickup signal 2 dB less than that of a sensor oriented along the Earth's field.
5. An experiment has been performed to determine the reduction in the free precession relaxation time  $T_2$  due to magnetic gradients from a magnetic moment. The results agree with theory.
6. A magnetic dipole detection test has been performed in which a  $10^5$  G-cm $^3$  magnet was successfully detected at a range of 150 feet by a  $^3\text{He}$  gradiometer of 13.33 foot separation.

## SECTION 7 RECOMMENDATIONS

The present contract effort represents the third phase of an effort (see Table 7.1) to develop the  $^3\text{He}$  free precession gradiometer for use in a mine application. Recommendations for the next phase of effort include the following:

1. Develop marine package for sensors.
2. Develop deployment package.
3. Develop a Wet Test sensor system.
4. Develop a data acquisition system.
5. Integrate sensor system with MODAB.
6. Plan and perform Wet Test.
7. Analyze noise and signal data and predict MAD subsystem performance.

TABLE 7.1. PROGRAM TASKS OUTLINE

Phase I

1. Measure S/N for various cells.
2. Measure free precession relaxation time ( $T_2$ ) for various cells, and pumping time ( $T_1$ ) for various cells and discharge levels.
3. Begin magnetometer analysis.
4. Calculate possible range.

Phase II

1. Determine optimum lamp pressure and the effect of multiple lamps on magnetometer sensitivity.
2. Increase free precession relaxation time.
3. Construct  $^3\text{He}$  magnetometer system and measure its sensitivity using several frequency discrimination techniques.
4. Develop simple detection algorithm and use it in a magnetometer system experiment to find the range at which a magnetic dipole of known strength moving in a straight line past the magnetometer system may be detected.

TABLE 7.1 (CONTINUED)

Phase III

1. Construct and evaluate an experimental development model of the  $^3\text{He}$  gradiometer which operates in nonequatorial latitudes (where the magnetic dip angle is 55 degrees or greater).
2. Determine effect of magnetic gradients on the operation of the  $^3\text{He}$  magnetometer.
3. Perform range experiments with magnetic dipole of known strength.
4. Determine orientation dependence of  $^3\text{He}$  magnetometer.

APPENDIX A  
WORK STATEMENT

A.1 Sensor Design

- Lamps and cell design -- Past  $^3\text{He}$  magnetometer data on lamps and cells of various shapes and pressures will be reviewed in order that the XDM lamp and cell design may be made. The optics to collect the lamp light and direct it into the cell will be designed.
- Pickup coil and flipping coil design -- The magnetic pickup coil and the moment-rotation coil will be designed. Experiments with pickup coils of several designs may be necessary.

A.2 Electronics Design

- Automatic pumping and flip -- Circuitry will be designed to light the cell and the lamp discharges for a given time (pumping), and to extinguish the discharges and rotate the cells' polarization (flipping).
- Automatic frequency lock-on -- The phase-lock-loop frequency discriminator's voltage-controlled oscillator must be locked onto the  $^3\text{He}$  pickup coil signal. Electronic means to do this automatically will be devised.
- Miscellaneous electronics modification -- Appropriate modifications of the present lamp oscillators, ignition oscillator (for cell discharge), and amplifiers will be performed.

#### A.3 System Construction

- Sensor construction -- The two magnetometers will be designed and built. Attention will be given to use of nonmagnetic materials.
- Electronics construction -- The support electronics will be constructed and hooked up to the sensors. A series of preliminary tests will be performed to ready the system for experimental use.

#### A.4 System Characterization Tests

- Internal parameter measurements -- Various internal parameters (such as initial pickup coil signal levels, transverse relaxation rates, etc.) will be included in this documentation.
- System sensitivity -- The gradiometer output noise level for several orientations will be measured. The variation of noise level with time will be found.
- Proximity of magnetic moment -- Performance degradation due to the proximity of a magnetic moment to the gradiometer will be investigated.
- Detection tests -- A moving target will be simulated by moving a magnet in a straight-line course by the gradiometer. Detection signal processing will be performed with the available computer (HP-9835).

#### A.5 Deliverables

- Monthly letter reports and a final report will be written.

APPENDIX B  
3He GRADIOMETER PERFORMANCE ANALYSIS  
METHODOLOGY

B.1 INTRODUCTION

This appendix deals with  $^3\text{He}$  gradiometer performance analysis which is based on a variation of the Quadratic Threshold Detector as is given by Reference 6, Chapter VII, Section 2. Section 2 of this appendix covers the general statistical theory of the approach; Section 3 contains the application of this theory to the  $^3\text{He}$  gradiometer for performance prediction purposes; Section 4 treats the application of the theory to the experimental data taken at the Texas Instruments Magnetic Test Site, Sherman, Texas, on January 6, 1982, which is described in more detail in the main body of this report. Overall, the results of the analysis of the experimental data agreed well with the theoretical predictions.

B.2 GENERAL STATISTICAL THEORY

A time series  $y_j = s_j + n_j$ , which is the output of a bandpass filter with band  $f_0$  to  $f_1$ , is assumed to be given where  $s_j$  is due to a target of interest and  $n_j$  is uncorrelated Gaussian noise. A moving window  $y_{j1}, \dots, y_{jJ}$ , consisting of  $J$  consecutive data points, is the basis for the random variable  $\epsilon$  defined by

$$\epsilon = \sum_{j=1}^J y_{jJ}^2.$$

The random deviate  $x = \sum_{j=1}^J n_j^2$  has a scaled chi-square distribution with  $v$  degrees of freedom; i.e.,  $x = \rho x_v^2$  with  $v = 2f_1 J \Delta t$ , where  $\Delta t^{-1}$  is the sampling rate, and  $\rho = \sigma_x^2/2 \mu_x$ .

The null hypothesis is  $s = 0$ , or equivalently, no target is present. Hence, the critical value for the probability of false alarm  $x_{p_{FA}}$  is given by

$$x_{p_{FA}} = \rho x_v^2, \quad p_{FA},$$

where  $x_v^2$ ,  $p_{FA}$  is the critical value of the probability  $p_{FA}$  for the chi-square distribution with  $v$  degrees of freedom.

In order to give the background for probability of detection, it is convenient to express all parameters of interest in terms of power density spectra. To this end let the noise PDS be denoted by  $\phi(f)$ , and the target PDS by  $H(f, \bar{q})$ , where  $f$  is a non-negative frequency and  $\bar{q}$  is a scenario vector. Also, let  $W(f)$  denote the band-pass filter normalized response function. Then it follows that

$$\mu_x = 2 J \int_0^{\infty} \phi(f) W(f) df$$

$$\sigma_x^2 = 2 \mu_x^2 / v,$$

where  $v = 2f_1 J \Delta t$ . Under the assumption that the signal and noise are uncorrelated, the probability of detection,  $P_D$ , is defined by the equation

$$x_v^2, P_D = \rho^{-1} [x_{p_{FA}} - 2 \int_0^{\infty} H(f, \bar{q}) W(f) df].$$

Performance analysis is conducted by determining  $P_D$  as a function of one or more critical components of  $\bar{q}$ . Analysis of experimental data is carried out by computing unbiased estimates for  $\mu_x$ ,  $\sigma_x$  and then calculating  $v$ ,  $\rho$ .

### B.3 $^3\text{He}$ GRADIOMETER PERFORMANCE PREDICTION

One possibility for performance prediction of the  $^3\text{He}$  gradiometer is given in this section. This particular version deals with detection range at CPA for  $P_d$  of 0.5 as a function of target velocity. Two approaches to determining the filter band are considered; the first varies the band width and center as a function of the ratio target velocity over range at CPA; the second uses a fixed band 0.004 - 0.009, which is the band where the  $^3\text{He}$  gradiometer noise spectrum has minimum energy relative to the bandwidth and is the effective matched filter band-pass for the experiment scenario.

A distinction between the two band-pass approaches is evident in Figure B-1. For the variable band-pass, approximately one half the target signal energy passes through the band at each velocity by design; however, for the fixed band-pass 0.004 to 0.009 Hz, no target signal energy passes through the band, based on the model, for the target velocity below 2.25 knots where the moment magnitude is  $3.5 \times 10^5 \text{ r-ft}^3$ . The fixed band gives a better performance prediction where it is defined.

The experiment CPA was 150 feet, so the curves in Figure B-1 indicate that the  $P_d$  should be well above 0.5. This is indeed the case, as is discussed in Section 4 of this appendix. The curves in Figure B-1 are based on a fixed scenario which was selected to be as much like the experiment scenario as possible.

### B.4 EXPERIMENTAL DATA RESULTS

This section deals with the statistical characterization of the noise encountered during the experiment conducted on January 6, 1982, and a comparison with a target signal on the same date for detection purposes. Results given here are for two filter bands, namely 0.0106 - 0.0212, and 0.004 - 0.009; a discussion of the two bands can be found in Section 3 of this appendix. Two intervals of noise data are used herein, one from approximately 4:50 P.M. to 5:45 P.M., and the other from approximately 6:10 PM to 7:00 P.M. In each case, processing was carried out by summing the squares of non-overlapping sixty data point windows which were moved through the noise data. The precise definition of the four combinations, C-1, C-2, C-3, and C-4, are defined in Table B.1.

### $^3\text{He}$ Performance Prediction Curves

Moment Magnitude:  $3.5 \times 10^5 \text{ dy-ft}^3$

PFA:  $10^{-6}$

Scenario: Approximately that of Experiment

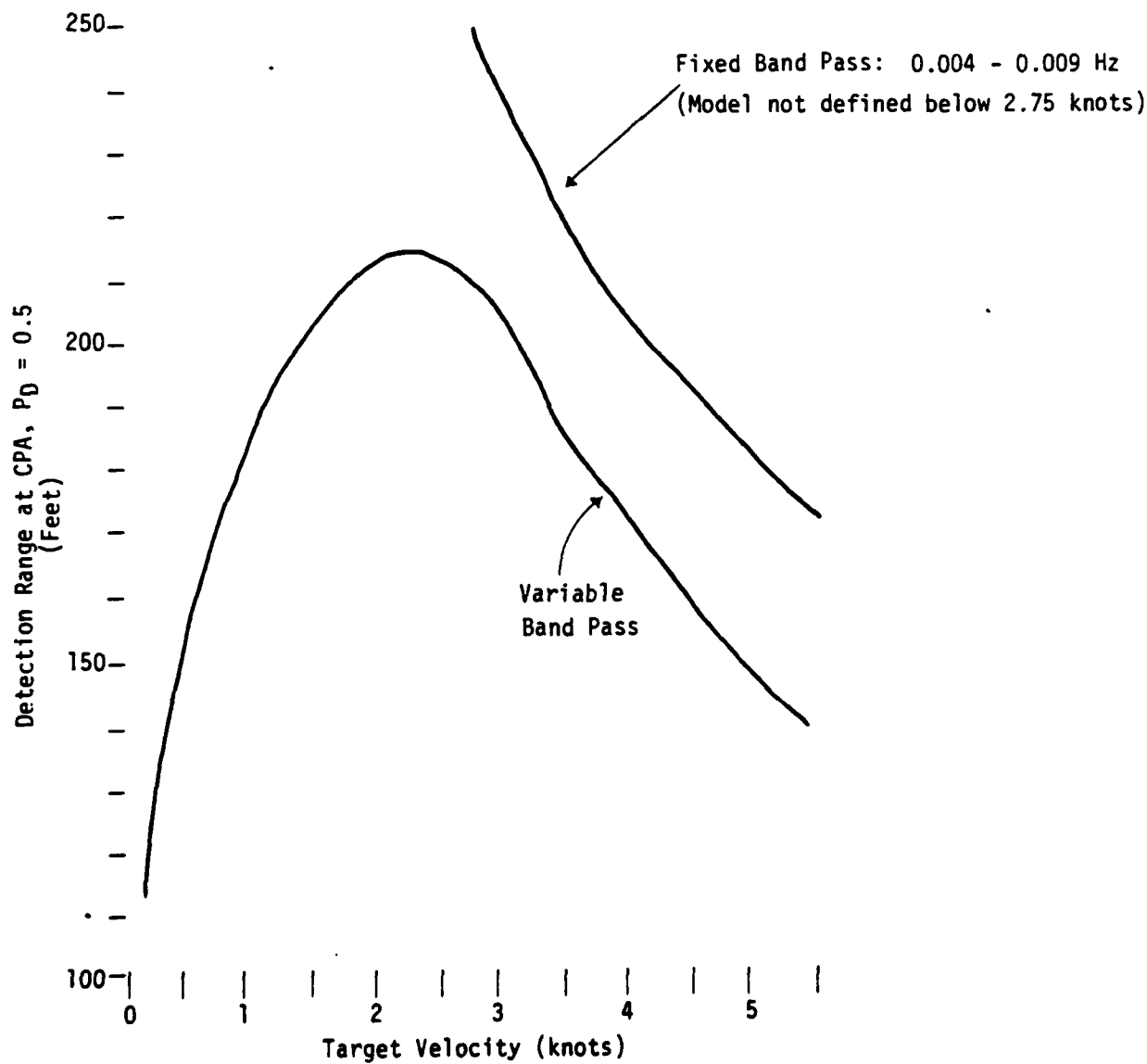


FIGURE B-1

TABLE B.1

Combination	Band Pass	Noise Time Interval	Sample Size
C-1	0.0106 - 0.0212	4:49:55 - 5:43:55	54
C-2	0.0106 - 0.0212	6:10:05 - 7:01:05	51
C-3	0.0040 - 0.0090	4:49:55 - 5:43:55	54
C-4	0.0040 - 0.0090	6:16:05 - 7:02:05	46

Statistical analysis consisted of computing  $\bar{x}$ ,  $s_x^2$ , the sample mean and sample variance for each of the four combinations C-1, C-2, C-3, C-4, and from these values estimating  $v$ ,  $\rho$  by setting  $v$  to be the integer nearest  $2\bar{x}^2/s_x^2$  and  $\rho = x/v$ . Next, a goodness-of-fit test was performed to check the agreement of the sample distribution with the theoretical distribution  $p_{Xv}^2$ . In addition, critical values for one false alarm per hour, two false alarms per hour, and one false alarm per day were calculated and applied to the sample distributions. Finally, these critical values were compared to the test statistic values computed during the target encounter which occurred from approximately 4:25:00 to 4:25:45 in order to determine if the detection condition was satisfied, which should be the case, according to the curve in Figure B-1.

The results of estimating  $v$ ,  $\rho$ , and of the 95% confidence level goodness-of-fit between the theoretical and sample distribution for the four combinations, are given in Table B-2, which shows high correlation between the two sets of noise data. Also, the estimates for  $v$  coincide with the values predicted by  $v = 2f_1 J \Delta t$ .

TABLE B.2

Combination	v	$\rho$	95% Fit
C-1	3	$1.29 \times 10^{-5}$	Yes
C-2	3	$1.30 \times 10^{-5}$	Yes
C-3	1	$5.93 \times 10^{-6}$	Yes
C-4	1	$7.80 \times 10^{-6}$	Yes

As a further test of the goodness-of-fit, theoretical critical values for the three false alarm rates mentioned above are given in Table B.3 along with the results of comparing them with the corresponding sample distributions. Again, close agreement is the case, particularly considering the small sample size.

TABLE B.3

Combination	False Alarm Rate	$P_{FA}$	Theoretical Critical Value $x_{P_{FA}}(\gamma^2)$	Sample Occurrences Past $x_{P_{FA}}$	Maximum Expected Occurrences Past $x_{P_{FA}}$
C-1	2/hour	$3.33 \times 10^{-2}$	$1.13 \times 10^{-4}$	1	1.80
	1/hour	$1.67 \times 10^{-2}$	$1.32 \times 10^{-4}$	0	0.90
	1/day	$6.94 \times 10^{-4}$	$2.20 \times 10^{-4}$	0	1.00
C-2	2/hour	$3.33 \times 10^{-2}$	$1.13 \times 10^{-4}$	3	1.70
	1/hour	$1.67 \times 10^{-2}$	$1.33 \times 10^{-4}$	1	0.85
	1/day	$6.94 \times 10^{-4}$	$2.22 \times 10^{-4}$	0	1.00
C-3	2/hour	$3.33 \times 10^{-2}$	$2.68 \times 10^{-5}$	2	1.80
	1/hour	$1.67 \times 10^{-2}$	$3.39 \times 10^{-5}$	2	0.90
	1/day	$6.94 \times 10^{-4}$	$6.82 \times 10^{-5}$	0	1.00
C-4	2/hour	$3.33 \times 10^{-2}$	$3.53 \times 10^{-5}$	0	1.53
	1/hour	$1.67 \times 10^{-2}$	$4.47 \times 10^{-5}$	0	1.77
	1/day	$6.94 \times 10^{-4}$	$8.98 \times 10^{-5}$	0	0.00

The values of the test statistic computed during the target encounter from approximately 4:25:00 to 4:25:45 are given in Table B.4. These values can be compared with the theoretical critical values in column 4 of Table B.3 in order to determine detection status. Although the encounter occurs primarily during the first one-minute window in Table B.4, the respective band-pass filters delay the signal so that maximum energy occurs in the third window for the filter with band 0.0106 - 0.0212 Hz, and in the fourth window for the filter with band 0.004 - 0.009 Hz.

TABLE B.4

Window Start Time	$\epsilon = \sum_{j=1}^{60} y_j^2 (\gamma^2)$	
	Band 0.0106 - 0.0212	Band 0.004 - 0.009
4:24:55	$1.35 \times 10^{-4}$	$2.74 \times 10^{-5}$
4:25:55	$1.32 \times 10^{-3}$	$1.34 \times 10^{-4}$
4:26:55	$1.65 \times 10^{-3}$	$6.85 \times 10^{-4}$
4:27:55	$3.02 \times 10^{-4}$	$7.95 \times 10^{-4}$
4:28:55	$1.21 \times 10^{-4}$	$4.93 \times 10^{-4}$

## REFERENCES

1. McGregor, D.D., "Final Report - Investigation to Improve the  $^3\text{He}$  Magnetometer for use in a Mine Application," Contract N60921-80-C-0161, Texas Instruments Incorporated, 22 May 1981.
2. McGregor, D.D., "Final Report - Investigation of  $^3\text{He}$  Free Precession Magnetometer for Mine Application," Contract N60921-79-C-0081, Texas Instruments, Incorporated, 24 December 1979. (Secret)
3. Slichter, C.P. Principles of Magnetic Resonance. New York: Harper & Row, Publishers, Incorporated, 1963.
4. Papoulis, A. Probability, Random Variables and Stochastic Processes. New York: McGraw-Hill Book Company, 1965. p. 505.
5. Chapman, S. and T.G. Cowling. The Mathematical Theory of Non-Uniform Gases. Second edition. Cambridge: Cambridge University Press, 1952.
6. Helstrom, C.W. Statistical Theory of Signal Detection. Second Edition. New York: Pergamon Press, 1968.